Simulation study of laser-driven ion acceleration: target-normal-sheath-acceleration using double-layer target, shock ion acceleration via relativistic transparency

Young-Kuk Kim

Department of Electrical and Computer Engineering

Graduate School of UNIST

Simulation study of laser-driven ion acceleration: target-normal-sheath-acceleration using double-layer target, shock ion acceleration via relativistic transparency

A thesis
submitted to the Graduate School of UNIST
in partial fulfillment of the
requirements for the degree of
Doctor of Philosophy of Science

Young-Kuk Kim

7. 8. 2016

Approved by

_____
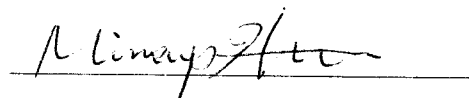
Advisor

Min Sup Hur

Simulation study of laser-driven ion acceleration: Target-normal-sheath-acceleration using double-layer target, shock ion acceleration via relativistic transparency.

Young-Kuk Kim

This certifies that the thesis of Young-Kuk Kim is approved.

6. 8. 2016
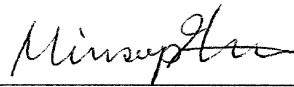
_____
Advisor: Min Sup Hur
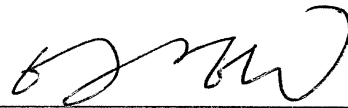
_____
Committee Member: Ki Tae Lee

_____
Committee Member: Eun Mi Choi

_____
Committee Member: Kyu Jin Kwak
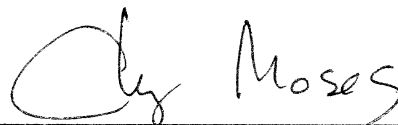
_____
Committee Member: Mo Ses Chung

Abstract

Laser-driven ion acceleration has become a major research topic after development of intense laser pulse. It is expected to replace a big conventional accelerator and generate pulsed ion beams with low emittance, high peak current. People have tried to enhance beam energy and collect ions into the intended energy range.

In this thesis, we introduce background knowledge for understand laser-driven ion acceleration. And we show the independence between the areal density of the second layer and the thickness of the first layer in target-normal-sheath-acceleration using double layer target. This result will serve valuable information when design the double layer target. And last, the electrostatic shock ion acceleration by a circularly polarized pulse via relativistic transparency will be presented. When a circularly polarized pulse drives shock, it is expected higher hole-boring velocity and higher ion beam energy.

Contents

List of Figures

List of Tables

I. Introduction

As the laser intensity increases on behalf of the chirped pulse amplification (CPA) technic [1], particle acceleration using an ultra-short and an ultra-intense laser pulse has been paid attention for a replacement of the conventional particle accelerators such as Linac, Cyclotron, and Synchrotron. Well organized PW class laser system has a room size but the conventional accelerators require a large size of system. Nowadays, 1 PW laser system is commercially available. In the near future, PW class laser systems would be inexpensive and stable.

The reason what I mentioned above PW laser system is that when the laser pulse peak power is reached PW level predicted maximum proton beam energy is about 200 MeV, which beam energy is available in proton therapy [2-4]. The cyclotron accelerator is currently used for the proton therapy, where proton beam transportation system (GANTRY) has a big portion of construction cost. Laser-ion accelerator pursuits replacing the expensive GANTRY system with vacuum laser beam path. Moreover energetic ion beam can be applied to various applications such as proton imaging [5], radiography [6], neutron production [7], isotope production [8, 9], ion injection source for conventional accelerator [10], biology, lithography, etc. and intense laser-plasma interaction itself is important to understand fast ignition [11], hot electron generation [12], astrophysics, shock [13], etc.

Although the laser peak power has been exceeded PW level, unfortunately, the maximum proton beam energy has not been reached 100 MeV. Furthermore, accelerated proton beam energy has 100% energy spread, which beam cannot be directly employed to the proton therapy. It is prospected that proton beam energy will overcome 200 MeV as improvement of the laser technology, acceleration scheme, and experiment condition but energy spread could not be suppressed less than 1% due to high temperature (~MeV) during the intense laser-plasma interaction. Therefore, energy selection system such as aperture system [14] would be required for proton therapy by laser-ion acceleration system.

Accelerated ion beams by the laser pulse have high peak current (~kA), very short beam duration (~fs) and very small emittance (~0.001 mm rad) [15] but low average current in comparison with a conventional accelerator. And *pulsed* ion beam is a distinguishing feature. The future of laser-driven ion acceleration area is dependent on finding out an application of above distinguishing ion beam properties.

There are two main research goals in the laser-ion acceleration; the one is an increase in ion beam energy and the other is a generation of mono-energetic ion beam. For research goals, laser intensity, duration, polarization, contrast ratio, double pulse, pulse shape and target thickness, density, structure, multi-layer, multi-species etc. have been being subject of experimental variables. In the early 2000s, linearly polarized laser pulse irradiated on the thick (10~100 μm) solid (>100n_c) target with square shape [16-20]. In order to understand experiment results target-normal-sheath-acceleration (TNSA) model has been accepted main acceleration scenario [21-25]. It has been known that maximum proton

energy increases as laser intensity increases and target thickness decreases in those days. In the middle 2000s, monoenergetic ion beam with few MeV was demonstrated in experiments [26, 27], where double layer target was adopted, and laser-driven ion acceleration got a lot of attention. However, people have tried to find another laser-target configuration because of low energy conversion efficiency $\propto \sqrt{I}$ in TNSA.

Naturally, radiation pressure dominant acceleration (RPDA) had arisen next laser-driven acceleration regime due to its high energy conversion efficiency ($\sim I$) and generation of monoenergetic ion beam, where a circularly polarized laser pulse and ultra-thin (1~10 nm) target are utilized in RPDA [28-37]. In the late 2000s, the first RPDA experiment was demonstrated [38] and it had been became an intensive research topic. Although theory and simulation about RPDA were intensively studied [39-44], experiment was rarely done because it requires strict high contrast ratio and normal laser incidence angle to the target.

In order to overcome low conversion efficiency of TNSA and experimental difficulty of RPDA, ion acceleration in near-critical density plasma has been paid attention. There are three acceleration regimes in near-critical density plasma ($n=1\sim10n_c$); electrostatic shock ion acceleration [45], magnetic vortex acceleration [46-48], and break-out afterburner [49, 50]. In point of fact, these regimes were minor acceleration scenario in comparison with TNSA or RPDA until the early 2010s. However, they have been being moving into main acceleration regime due to development of near-critical plasma generation methods, for example, control of pre-pulse or ASE, another single pulse irradiation, high density gas jet [51], Z-pinch [52], liquid crystal target [53], etc.
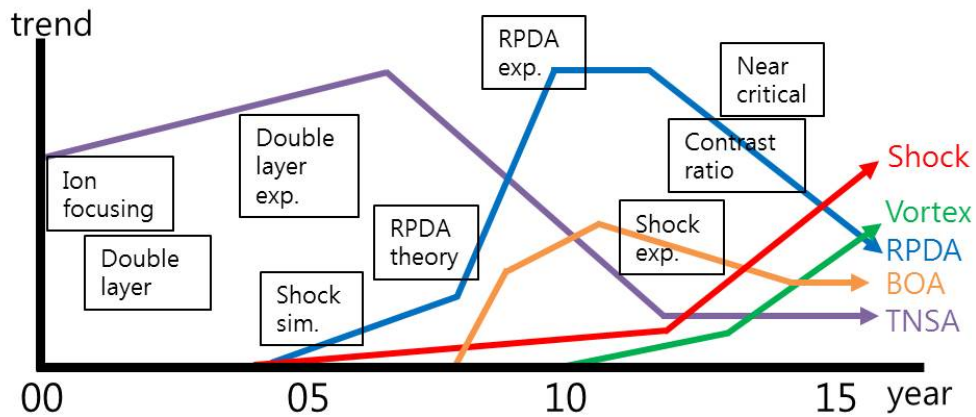
Fig. 1.1: Trend of laser-driven ion acceleration regimes. Boxes represent important issues at that time.

II. Background

2.1. Temperature

In plasma physics, the temperature mainly indicates electron temperature. The temperature represents particle velocity dispersion. Plasma with low velocity dispersion of electron has low temperature but plasma with high velocity dispersion of electron has high temperature. Note that a group particle with high velocity (high energy) does not mean high temperature. For example, particle beam with average velocity 0.9c and velocity dispersion 0.01c has high kinetic energy and low temperature but particle beam with average velocity 0.01c and velocity dispersion 0.9c has low kinetic energy and high temperature.

The Maxwellian distribution is a typical tool for describing temperature of a thermal equilibrium system. The one- and three-dimensional Maxwellian distribution are given by [54]

$$f(v) = n\sqrt{\frac{m}{2\pi KT}} \exp\left(-\frac{mv^2}{2KT}\right) \tag{1}$$

$$f(v_x, v_y, v_z) = n\left(\frac{m}{2\pi KT}\right)^{1.5} \exp\left(-\frac{m(v_x^2 + v_y^2 + v_z^2)}{2KT}\right) \tag{2}$$

where f(v) is particle distribution function, m is particle mass, n is density, K=1.38 x 10^{-23} J/K is Boltzmann's constant, T is temperature, and v is velocity.

A relationship between average particle kinetic energy and temperature is useful to calculate temperature in PIC simulation. The relationship is given by

$$E_{av} = \frac{3}{2}KT \quad \text{or} \quad KT = \frac{2}{3}\frac{\sum_i^N (\gamma_i - 1)mc^2}{N} \tag{3}$$

, where N is the number of total particle and $(\gamma - 1)mc^2$ is the particle kinetic energy.

Unfortunately, the average kinetic energy does not represent multi-temperature system exactly. In multi-temperature system, for example two-temperature cases T_c=1eV and T_h=10eV and each particle number is same, the temperature calculated by the average kinetic energy T=5.5eV does not describe two-temperature T_c and T_h of system. In this case combination of the Maxwellian distribution function should be fitted to the particle velocity distribution. I recommend that a use of the Maxwellian distribution for the energy E given by

$$f_E(E) = 2\sqrt{\frac{E}{\pi}}\left(\frac{1}{KT}\right)^{1.5} \exp\left(-\frac{E}{KT}\right) \tag{4}$$

, which function can be employed to the energy spectrum directly. In most of papers in laser-ion acceleration represent temperature in the energy spectrum graph.
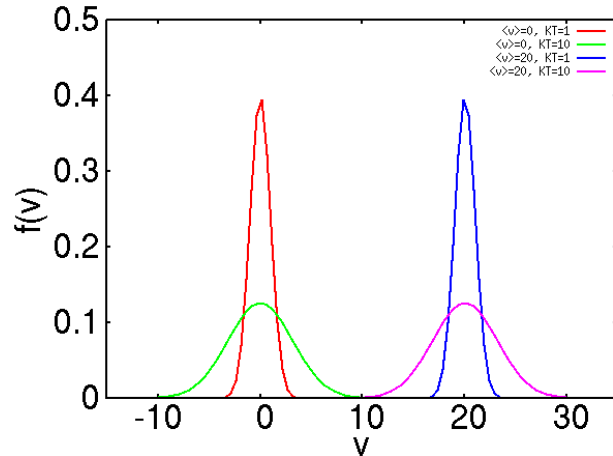
Fig. 2.1.1: Temperature: red = blue < green = magenta. Average kinetic energy: green < red < blue < magenta.

When the electron velocity is closed to the speed of light c, the Maxwellian distribution cannot represent temperature of relativistic plasma. In relativistic plasma, a difference of electron velocity is almost 0 ($dv = v_1 - v_2 \sim 0$) but a difference of electron kinetic energy $dk = (\gamma_1 - \gamma_2)mc^2$ is finite value. Therefore, it is reasonable that a distribution function is described as relativistic gamma γ rather than velocity v in relativistic temperature plasma.
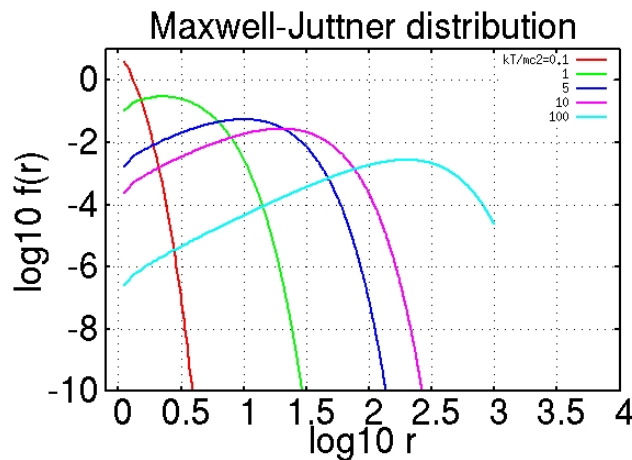
Fig. 2.1.2: Maxwell-Juttner distribution for θ=0.1, 1, 5, 10, 100 plasmas, which are equivalent to temperature of 51 keV, 510 keV, 2.6 MeV, 5.1 MeV, and 51 MeV.

Maxwell-Juttner distribution function was developed to describe relativistic plasma. The function is given by

$$f(\gamma) = \frac{\gamma^2 \beta}{\theta K_2(1/\theta)} \exp\left(-\frac{\gamma}{\theta}\right) \qquad (5)$$

, where β=v/c=$\sqrt{1-1/\gamma^2}$, $\theta = kT/mc^2$, K_2 is the modified Bessel function of the second kind.

4

2.2. Debye sheath

A formation of the Debye sheath is a nature of charged particles, which tend to become a charge neutral state. When a positively charged region (the number of ions is larger than the number of electrons) exists in a plasma, negatively charged particles (electrons) are attracted to the positively charged region from an outside of it. The attraction between the positively charged region and nearby electrons is done until a net become charge neutral state. In most case, heavy ions are regarded as a fixed particles but light electron is regarded as a freely moving particle. Therefore, 'the sheath' frequently points out 'the electron sheath' in plasma physics.

The sheath field is formed between the positively charged region and the sheath, which field attracts electron to the positively charged region and ion to the negatively charged region. When the positively charged region is a sphere and the sheath is formed its outside as a spherical shell, sheath field intensity is linearly increased to the radial direction in the positively charged region and it is exponentially decreased in the sheath region. Therefore, ions are expanded by the non-uniform electro-static sheath field, where ions on the boundary of the sphere get highest velocity.

The Debye length λ_D is defined to represent the sheath length, which length indicates that the position of sheath potential down to the e^{-1} with respect to the potential on the plasma boundary. The Debye length is given by [54]

$$\lambda_D = \sqrt{\frac{\varepsilon_0 K T_e}{ne^2}} \tag{6}$$

, where $\varepsilon_0 = 8.854 \times 10^{-12} \, F/m$ is the permittivity of free space. Obviously, the Debye length is the function of temperature and density. As the temperature increases, the electron sheath cloud should be expanded for a same potential because many electrons could have sufficiently high kinetic energy to escape the sheath potential. When the density increases, many electrons are concentrated in space, the sufficient number of electrons is in a short Debye length to shield the potential.

In order to observe the Debye sheath clearly, a finite plasma and temperature are required. In laser-ion acceleration, plasma always has a finite thickness and a few MeV temperatures due to the heating by an intense laser pulse. The electron sheath naturally formed outside of the plasma. The expansion by the sheath field is the source of ion acceleration in Target Normal Sheath Acceleration (TNSA) regime. However, most of ion acceleration regimes have tried to avoid the sheath field effect because the sheath field stretches ion beams in phase space; ion beam energy spectrum is broadened by the sheath field.

Computational issue

It is difficult to resolve the initial Debye length for an over dense plasma. For example, simulation grid size should be decreased down to 0.3 nm to resolve the initial Debye length when the temperature

is cold about order of keV and the target is a Diamond-like-carbon (DLC), which has density order of $600n_c$. Cold plasma can be considered before the arrival of the main pulse on the target. In order to avoid a very short initial Debye length, initial density and temperature are arbitrary adjusted in simulation. A slightly overdense (a few n_c) and uniform plasmas were frequently used to increase the initial Debye length in the early laser-ion acceleration simulation. As a computational capacity has been improved, a realistic simulation can be done using a supercomputer. However, a small simulation groups are staying in a parameter range in $10\sim100n_c$ and $1\sim100$ keV.

KT (keV) \ n (n_c)	0.1	1	10	100	600
1	22.2 nm	7.0 nm	2.2 nm	0.7 nm	0.3 nm
10	70.3 nm	22.2 nm	7.0 nm	2.2 nm	0.9 nm
100	222.3 nm	70.3 nm	22.2 nm	7.0 nm	2.9 nm
1000	702.9 nm	222.3 nm	70.3 nm	22.2 nm	9.1 nm

Table 2.2.1: Debye length λ_D for a different density and temperature.

2.3 Ponderomotive force

A ponderomotive force is a source of various nonlinear phenomena in relativistic regime such as electron and ion acceleration. The ponderomotive force is given by

$$F_p = -\frac{e^2}{4m\omega^2}\nabla(E^2)\,. \tag{7}$$

Unlike electric and magnetic field, ponderomotive force is not relevant to the sign of charged particle. Negative electron and positive ion are forced to the same direction by ponderomotive force just as E x B drift [Textbook]. The direction of ponderomotive force is negative gradient of electric field square $-\nabla E^2$. This means that particle is forced from high intensity to low intensity region. For example, the direction of ponderomotive force of Gaussian pulse is radial.

The ponderomotive force is very weak in non-relativistic laser intensity. In non-relativistic regime $v \ll c$, charged particle (mainly electron) is oscillated to the transverse direction only following electric field oscillation of the laser pulse. As the laser intensity exceeds relativistic regime $a_0 > 1$, however, ponderomotive force becomes dominant because ponderomotive force is proportional to $-\nabla E^2$.

In a laser pulse region, which is underdense region, the motion of electron is represented as combination of oscillating transverse motion by electric field and longitudinal motion by ponderomotive force. In most cases, oscillating electric field could not displace particle position but ponderomotive force displaces particle from its original position.

On a laser pulse boundary, which is surface of overdence plasma, electron is instantly accelerated by strong ponderomotive force and weak electric field. The electron cannot show oscillating motion to the transverse direction and propagates to the longitudinal direction with small transverse velocity spread due to instant exposure to the transverse electric field.

The important point of ponderomotive force is an oscillation characteristic depending on the laser polarization. For linear and circular polarization, ponderomotive force is represented as

$$\vec{E} = E_0(x)\sin(\omega t)\vec{y}, \qquad \vec{F_p} = -\frac{e^2}{8m\omega^2}\nabla[E_0^{\ 2}(x)(1-\cos(2\omega t)] \quad \text{for linear} \tag{8}$$

$$\vec{E} = E_0(x)\sin(\omega t)\vec{y} + E_0(x)\cos(\omega t)\vec{z}, \qquad \vec{F_p} = -\frac{e^2}{4m\omega^2}\nabla[E_0^{\ 2}(x)] \quad \text{for circular} \tag{9}$$

In linearly polarized laser pulse, ponderomotive force is made up of slow varying portion by laser envelope and fast oscillating portion by half wavelength period 2ω. However, circularly polarized pulse has only slowly varying ponderomotive force. During $0 \sim \lambda/4$ wavelength of LP pulse irradiates on overdense plasma, ponderomotive force increases from 0 to its local maximum in Fig. 2.3.1. In this T/4 period, electrons in skin depth region are accelerated to the forward direction with velocity spread from 0 to maximum. During the next $\lambda/4 \sim \lambda/2$ period, electrons are accelerated to the forward direction with velocity spread from maximum to 0. At every $\lambda/2$ period, electrons are accelerated to
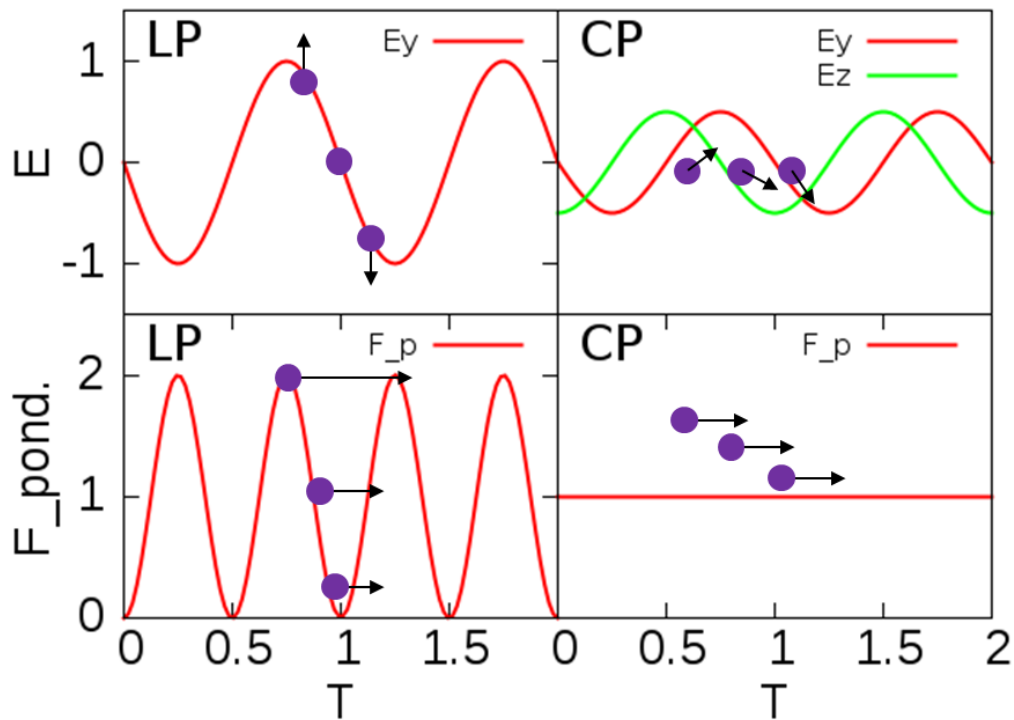
Fig. 2.3.1: Illustration of electric field and ponderomotive force of LP and CP pulse, where purple circle represent charged particle and T=2π/ω is laser period. Charged particle transversely oscillates by the electric field of LP pulse and transversely rotates by that of CP pulse. In a longitudinal motion, charged particle is periodically pushed by ponderomotive force with a large velocity spread when LP pulse irradiates. On the other hand, charged particle is continuously pushed by ponderomotive force with a small velocity spread when CP pulse irradiates. Note that averaged transvers motion is zero due to symmetric oscillation but averaged longitudinal motion is not zero.

the forward direction with high velocity spread, which means high temperature electron is supplied into the plasma by LP pulse. This process is called as ponderomotive heating or J×B heating.

On the other hand, electrons are continuously accelerated without velocity spread when CP pulse irradiates on overdense plasma due to absence of oscillating ponderomotive force. Instead, cold electrons are collimated on the laser irradiating surface and construct high density electron layer in plasma.

2.4 Prepulse (or ASE) and preplasma

Amplified spontaneous emission (ASE) means uncoherent wave amplified through a laser gain medium. When the uncoherent wave is chirped on the grating, it is broaden in background. If the chirped wave is amplified at the next stage, uncoherent waves will be amplified with long duration. A contrast ratio, which is the intensity ratio of main pulse to ASE, is widely used in order to represent ASE intensity. High contrast means low ASE and low contrast means high ASE.

ASE has received attention in laser-driven ion acceleration due to its high intensity over ionization level. Target deformation by ASE causes a significant problem because target thickness and density are varied before main pulse arrives, where pre-ionized plasma is called "preplasma". If there is no information about preplasma by ASE, we cannot understand what was happened during the interaction. It is hardship for designer to configure laser-target parameters.

There are two strategies to avoid preplasma effect; suppression of ASE and utilization of ASE. Contrast ratio has been suppressed progressively with year in order to avoid preplasma effect, even decreasing main pulse intensity. The state-of-the-art contrast ratio adopting double plasma mirror system is about $10^{11} \sim 10^{12}$ [55]. However a lot of laser systems with lower contrast ratio $< 10^{10}$ may cause preplasma. Thus some groups have tried to utilize intense ASE instead of suppressing that to generate intended plasma profile. They configure laser-target parameters considering pre-plasma profile.

Although preplasma profile could not be solved analytically, it was predicted using hydro-code simulations. Preplasma profile is influenced by ASE intensity, duration, target thickness, density and species mass. It is broaden when the ASE intensity and duration are large. And it becomes symmetry for an ultrathin target thickness but antisymmetric for a thick target thickness.
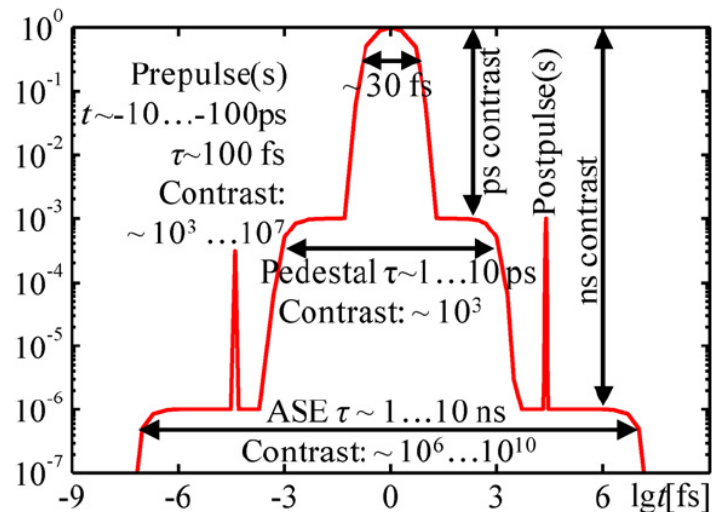
Fig. 2.4.1: Typical temporal structure of an intense ultra-short laser pulse with several kinds of preceding light. [56]
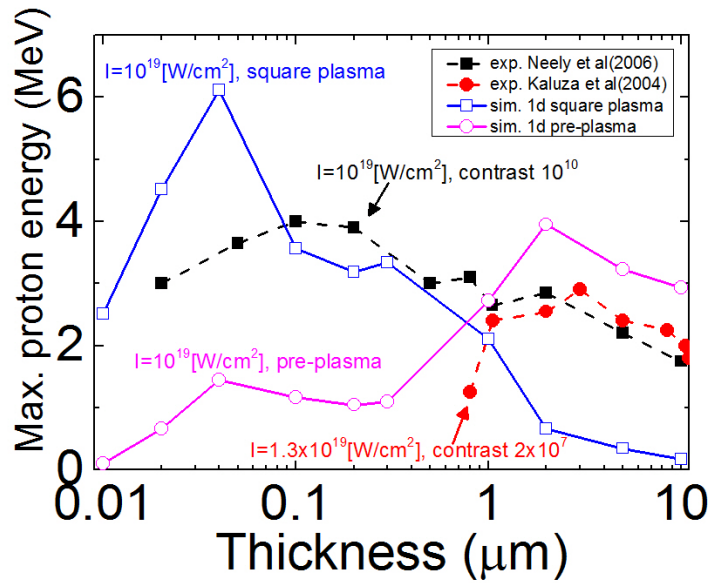
Fig. 2.4.2: A comparison of the maximum proton energy in TNSA simulation and experiment [57, 58] for a different thickness and contrast (in experiment) or preplasma state (in our simulation). When a high contrast ratio 10^{10} was used, maximum energy was produced around 0.1 μm thickness (black square and dashed line). Simulation for a square shape plasma shown generation of maximum energy around 0.04 μm thickness (blue opened square and solid line). On the other hand, proper thickness for generation of maximum energy was increased around 2-3 μm in experiment and simulation when contrast ration increases (preplasma exists in simulation).

In Fig. 2.4.2 illustrates a well-known example of preplasma effect in TNSA [59, 60]. When a high contrast ratio 10^{10} was used in experiment, maximum energy was produced around 0.1 μm thickness and simulation for square shape plasma shown generation of maximum energy around 0.04 μm thickness. On the other hand, proper thickness for generation of maximum energy was increased around 2-3 μm in experiment and simulation when contrast ration increases (preplasma exits in simulation). Therefore designer should make target thickness considering contrast ratio of laser system.

III. Particle-in-cell code

The particle-in-cell (PIC) code is widely used in laser-plasma simulation on behalf of its accurate calculation for non-linear and kinetic phenomena. PIC algorism solves Maxwell equation (E and B) and equation of motion for position and velocity (x and v) of every simulation particle at a given time (t) via finite-difference time-domain (FDTD) numerical method. In this chapter, I will briefly introduce basic FDTD method.
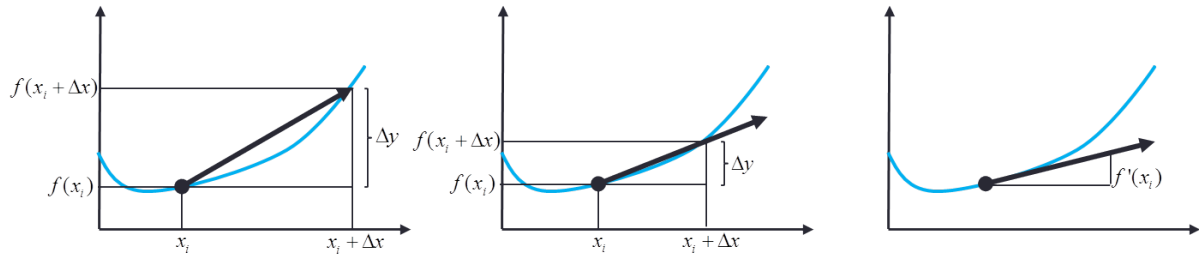
Fig. 3.1: Concept of finite-difference method [98].

In order to solve differential equation, a finite-difference (FD) method is adopted to differential equation set. The FD is represented as

$$\frac{\Delta y}{\Delta x} = \frac{f(x_i + \Delta x) - f(x_i)}{\Delta x}.$$ (10)

In Fig. 3.1, as a spacing Δx goes to 0 the difference approximation eq. (10) is closed to a derivative $\lim_{\Delta x \to 0} \frac{\Delta y}{\Delta x} = \frac{dy}{dx}$. Therefore small grid size Δx calculates more accurate numerical results.

Numerical error of FD is estimated by comparing derivative. The Taylor expansion of derivative at x_i is

$$f(x_{i+1}) = f(x_i) + f'(x_i)(x_{i+1} - x_i) + \frac{f''(x_i)}{2!}(x_{i+1} - x_i)^2 + \cdots + R_n = f(x_i) + f'(x_i)(x_{i+1} - x_i) + R_1$$

$$f'(x_i) = \frac{f(x_{i+1}) - f(x_i)}{x_{i+1} - x_i} - \frac{R_1}{x_{i+1} - x_i} = \underbrace{\frac{f(x_{i+1}) - f(x_i)}{h}}_{\text{First-order approximation}} - \underbrace{O(h)}_{\text{Truncation error}}$$ (11)

, where $h = x_{i+1} - x_i < 1$ and $O(h)$ is the first order truncation error.

When one solve the first derivative using the first order FD, a centered difference approximation is universally utilized due to the second order truncation error without computational cost. The graphical view is illustrated in Fig. 3.2 (Right), where the derivative position is located at the center between two points. It is represented as

$$f'(x_i) = \frac{f(x_{i+1}) - f(x_{i-1})}{2h} - O(h^2)$$ (12)
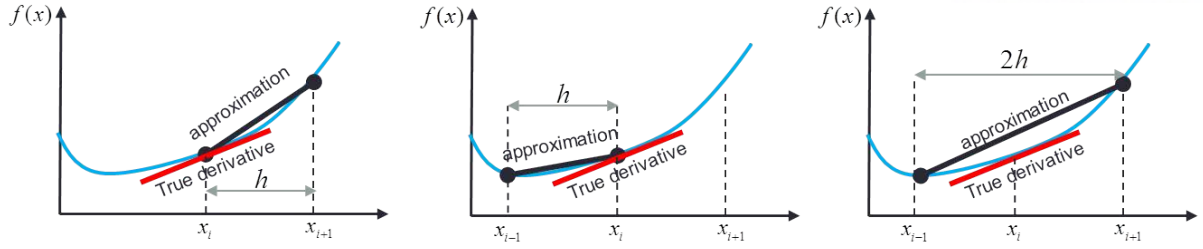
Fig. 3.2: (Left) Forward difference with O(h). (Middle) Backward difference with O(h). (Right) Centered difference with O(h^2) [98].

From now on, we will apply FD to Maxwell equations. Maxwell equations in a vacuum (J=0) are

$$\nabla \times E = -\frac{dB}{dt} \tag{13}$$

$$\nabla \times B = \frac{1}{c}\frac{dE}{dt}. \tag{14}$$

The equation set means a rotating E (or B) field generates rotating B (or E) field (see Fig. 3.3 (left)). After adopting FD to spatial and temporal derivatives in 3 dimension

$$(\nabla \times E)_x = (\frac{\partial E_z}{\partial y} - \frac{\partial E_y}{\partial z}) = -\frac{dB_x}{dt} \rightarrow \frac{E_z(y)-E_z(y-\Delta y)}{\Delta y} - \frac{E_y(z)-E_y(z-\Delta z)}{\Delta z} = -\frac{B_x(t)-B_x(t-\Delta t)}{\Delta t}$$

$$(\nabla \times E)_y = (\frac{\partial E_x}{\partial z} - \frac{\partial E_z}{\partial x}) = -\frac{dB_y}{dt} \rightarrow \frac{E_x(z)-E_x(z-\Delta z)}{\Delta z} - \frac{E_z(x)-E_z(x-\Delta x)}{\Delta x} = -\frac{B_y(t)-B_y(t-\Delta t)}{\Delta t}$$

$$(\nabla \times E)_z = (\frac{\partial E_y}{\partial x} - \frac{\partial E_x}{\partial y}) = -\frac{dB_z}{dt} \rightarrow \frac{E_y(x)-E_y(x-\Delta x)}{\Delta x} - \frac{E_x(y)-E_x(y-\Delta y)}{\Delta y} = -\frac{B_z(t)-B_z(t-\Delta t)}{\Delta t}$$

$$(\nabla \times B)_x = (\frac{\partial B_z}{\partial y} - \frac{\partial B_y}{\partial z}) = \frac{1}{c}\frac{dE_x}{dt} \rightarrow \frac{B_z(y)-B_z(y-\Delta y)}{\Delta y} - \frac{B_y(z)-B_y(z-\Delta z)}{\Delta z} = \frac{1}{c}\frac{E_x(t)-E_x(t-\Delta t)}{\Delta t}$$

$$(\nabla \times B)_y = (\frac{\partial B_x}{\partial z} - \frac{\partial B_z}{\partial x}) = \frac{1}{c}\frac{dE_y}{dt} \rightarrow \frac{B_x(z)-B_x(z-\Delta z)}{\Delta z} - \frac{B_z(x)-B_z(x-\Delta x)}{\Delta x} = \frac{1}{c}\frac{E_y(t)-E_y(t-\Delta t)}{\Delta t}$$

$$(\nabla \times B)_z = (\frac{\partial B_y}{\partial x} - \frac{\partial B_x}{\partial y}) = \frac{1}{c}\frac{dE_z}{dt} \rightarrow \frac{B_y(x)-B_y(x-\Delta x)}{\Delta x} - \frac{B_x(y)-B_x(y-\Delta y)}{\Delta y} = \frac{1}{c}\frac{E_z(t)-E_z(t-\Delta t)}{\Delta t}$$

$$(15)$$

Here, we used the FD to space (x, y, z) and time (t) domain. Therefore PIC code is the finite difference (FD) time domain (TD) numerical solver. For a rectangular grid system, rotating fields are represented as Fig. 3.3 (right).

In order to simplify convention for code implementation, the following representation is widely used.

$$\underset{\text{component}}{E_x}(\underset{\text{position}}{x,y,z,}\overset{\text{time}}{t}) \rightarrow E_x^n(x,y,z) \rightarrow E_x^n\underset{\substack{\text{Position}\\\text{(integer in a code)}}}{(i,j,k)} \tag{16}$$

Note that (i, j, k, n) are integer for code implementation. The converted version of FDTD set is
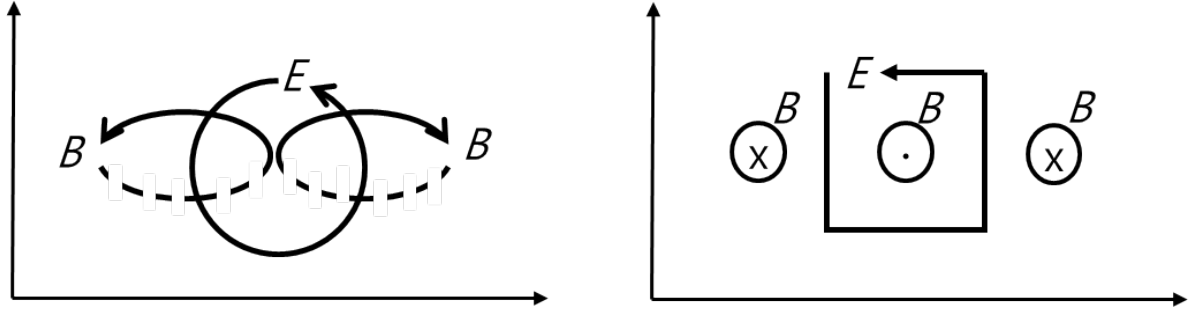
Fig. 3.3: (Left) Rotating fields in real space. (Right) Rotating fields in 2D grid space.

$$x : B_x^{n+\frac{1}{2}}(i, j+\frac{1}{2}, k+\frac{1}{2})$$

$$= B_x^{n-\frac{1}{2}}(i, j+\frac{1}{2}, k+\frac{1}{2}) - \frac{\Delta t}{\Delta y}[E_z^n(i, j+1, k+\frac{1}{2}) - E_z^n(i, j, k+\frac{1}{2})] + \frac{\Delta t}{\Delta z}[E_y^n(i, j+\frac{1}{2}, k+1) - E_y^n(i, j+\frac{1}{2}, k)]$$

$$y : B_y^{n+\frac{1}{2}}(i+\frac{1}{2}, j, k+\frac{1}{2})$$

$$= B_y^{n-\frac{1}{2}}(i+\frac{1}{2}, j, k+\frac{1}{2}) - \frac{\Delta t}{\Delta z}[E_x^n(i+\frac{1}{2}, j, k+1) - E_x^n(i+\frac{1}{2}, j, k)] + \frac{\Delta t}{\Delta x}[E_z^n(i+1, j, k+\frac{1}{2}) - E_z^n(i, j, k+\frac{1}{2})]$$

$$z : B_z^{n+\frac{1}{2}}(i+\frac{1}{2}, j+\frac{1}{2}, k)$$

$$= B_z^{n-\frac{1}{2}}(i+\frac{1}{2}, j+\frac{1}{2}, k) - \frac{\Delta t}{\Delta x}[E_y^n(i+1, j+\frac{1}{2}, k) - E_y^n(i, j+\frac{1}{2}, k)] - \frac{\Delta t}{\Delta x}[E_x^n(i+\frac{1}{2}, j+1, k) - E_x^n(i+\frac{1}{2}, j, k)] \qquad (17)$$

$$x : E_x^{n+1}(i+\frac{1}{2}, j, k)$$

$$= E_x^n(i+\frac{1}{2}, j, k) + \frac{c\Delta t}{\Delta y}[B_z^{n+\frac{1}{2}}(i+\frac{1}{2}, j+\frac{1}{2}, k) - B_z^{n+\frac{1}{2}}(i+\frac{1}{2}, j-\frac{1}{2}, k)] - \frac{c\Delta t}{\Delta z}[B_y^{n+\frac{1}{2}}(i+\frac{1}{2}, j, k+\frac{1}{2}) - B_y^{n+\frac{1}{2}}(i+\frac{1}{2}, j, k-\frac{1}{2})]$$

$$y : E_y^{n+1}(i, j+\frac{1}{2}, k)$$

$$= E_y^n(i, j+\frac{1}{2}, k) + \frac{c\Delta t}{\Delta z}[B_x^{n+\frac{1}{2}}(i, j+\frac{1}{2}, k+\frac{1}{2}) - B_x^{n+\frac{1}{2}}(i, j+\frac{1}{2}, k-\frac{1}{2})] - \frac{c\Delta t}{\Delta x}[B_z^{n+\frac{1}{2}}(i+\frac{1}{2}, j+\frac{1}{2}, k) - B_z^{n+\frac{1}{2}}(i-\frac{1}{2}, j+\frac{1}{2}, k)]$$

$$z : E_z^{n+1}(i, j, k+\frac{1}{2})$$

$$= E_z^n(i, j, k+\frac{1}{2}) + \frac{c\Delta t}{\Delta x}[B_y^{n+\frac{1}{2}}(i+\frac{1}{2}, j, k+\frac{1}{2}) - B_y^{n+\frac{1}{2}}(i-\frac{1}{2}, j, k+\frac{1}{2})] - \frac{c\Delta t}{\Delta y}[B_x^{n+\frac{1}{2}}(i, j+\frac{1}{2}, k+\frac{1}{2}) - B_x^{n+\frac{1}{2}}(i, j-\frac{1}{2}, k+\frac{1}{2})]$$

Note that the calculation time is different for E (n) and B ($n+1/2$). This is an intended time sequence for reduce numerical error in FDTD and called as leapfrog method (see Fig. 3.4).

And the E and B field are located at different position in conventional FDTD. In Fig. 3.5 and 3.6 illustrates field position on the cell.
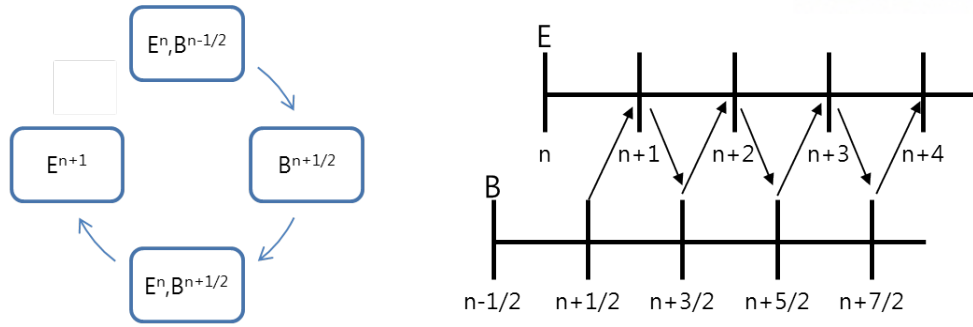
Fig. 3.4: Leapfrog method and sequence of field calculation.
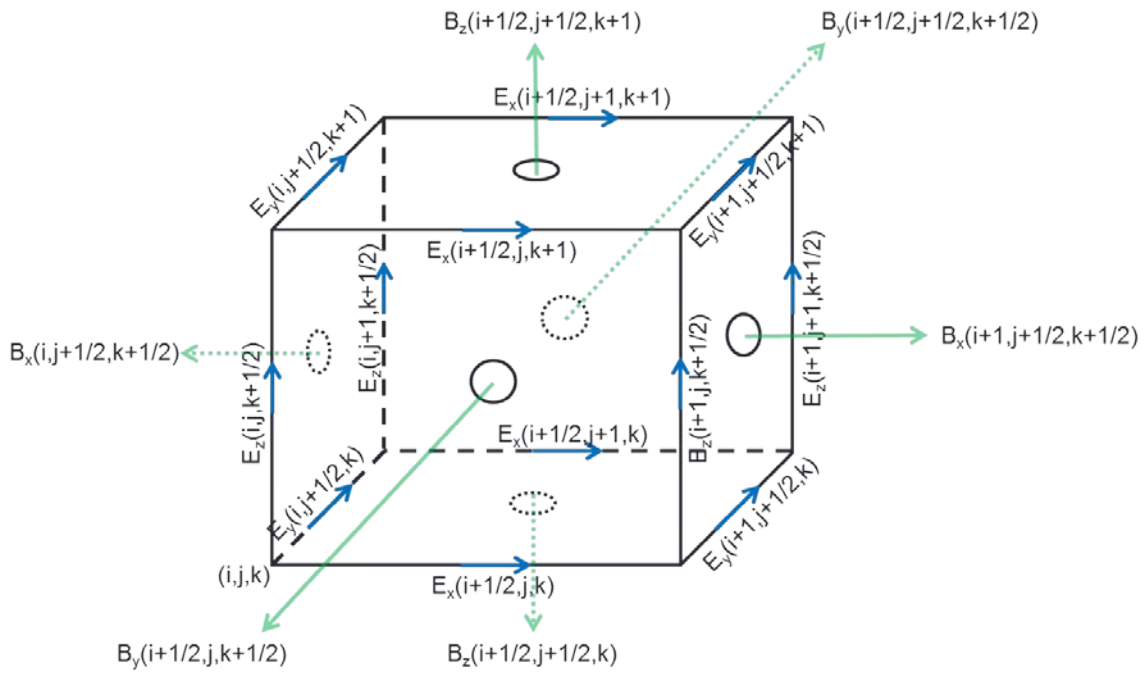
Fig. 3.5: E is located on the side and B field location on the surface. It is possible to exchange positions between E and B.
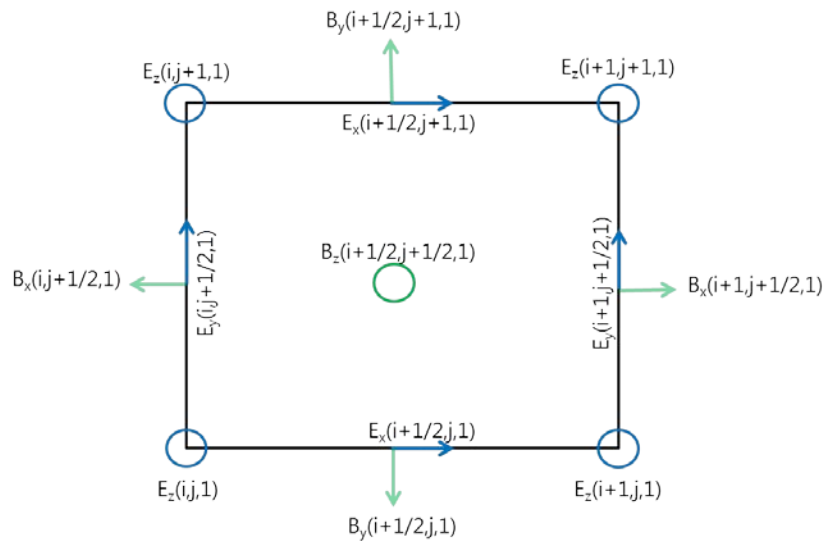
Fig. 3.6: Conversion of 3D cell of Fig. 3.5 into 2D cell.

14

Numerical error can be evaluated by comparing theoretical dispersion relation and numerical dispersion relation [99]. In free space, dispersion relation is given by

$$(\frac{\omega}{c})^2 = k_x^2 + k_y^2 + k_z^2 \tag{18}$$

, where k_x, k_y, and k_z are the propagation constants along the x, y, and z directions. For an arbitrary wave function $\zeta(x,y,z,t)=\zeta_0 exp[i(\omega t-k_x x-k_y y-k_z z)]$, numerical expression becomes

$$\zeta^n(I,J,K) = \zeta_0 \exp[i(\omega n\Delta t - k_x I\Delta x - k_y J\Delta y - k_z K\Delta z)] \tag{19}$$

Discretized version of dispersion relation in a free space can be got by inserting the numerical expression into wave equation by using the centered difference.

$$\left[\frac{1}{c\Delta t}\sin(\frac{\omega\Delta t}{2})\right]^2 = \left[\frac{1}{\Delta x}\sin(\frac{k_x\Delta x}{2})\right]^2 + \left[\frac{1}{\Delta y}\sin(\frac{k_y\Delta y}{2})\right]^2 + \left[\frac{1}{\Delta z}\sin(\frac{k_z\Delta z}{2})\right]^2 . \tag{20}$$

After solving the dispersion relation for ω, we get

$$\omega = \frac{2}{\Delta t}\sin^{-1}(c\Delta t\left[\frac{1}{\Delta x}\sin(\frac{k_x\Delta x}{2})\right]^2 + \left[\frac{1}{\Delta y}\sin(\frac{k_y\Delta y}{2})\right]^2 + \left[\frac{1}{\Delta z}\sin(\frac{k_z\Delta z}{2})\right]^2) . \tag{21}$$

Because ω must be a real value

$$\Delta t \leq \frac{1}{c\sqrt{\frac{1}{\Delta x^2} + \frac{1}{\Delta y^2} + \frac{1}{\Delta z^2}}} \tag{22}$$

This is called the Courant condition. The condition *must be* satisfied in any FDTD simulations.

IV. Acceleration regimes

4.1. Target normal sheath acceleration

4.1.1. Description

Target normal sheath acceleration (TNSA) scenario was developed to explain initial stage laser-target ion acceleration experiments. In experiments, accelerated ion beam shown thermal energy spectrum and cutoff energy at its maximum. And ion beam energy is increased as the target thickness is decreased. Although TNSA scenario is out of style in theoretical point of view, it is still important to do experiment in current available laser and target systems.

When a linearly polarized laser pulse irradiates on thick solid target (about 1~100 μm thickness were used at initial stage experiments and solid has density over $200n_c$), the pulse deeps into the target by skin depth. Electrons within the skin depth are accelerated to the forward direction by oscillating laser ponderomotive force. Because the laser ponderomotive force is periodic and continuous, accelerated electrons are periodically accelerated with 100% energy spread. These hot electrons penetrate into the quasi-neutral target without losing their energy. Although hot electrons are evacuated from the short skin depth region on the frontside of the target, a nearby cold electrons instantly fill skin depth region by electrostatic field during the laser ponderomotive force becomes small amplitude. This electron rearrangement supplies new electrons into skin depth region to be accelerated at the next laser ponderomotive force period.

When hot electrons arrived on the backside of the target, they instantly pass through the backside boundary. Then neutral backside of the target is ionized by the intense electrostatic field between hot electrons outside of the target and target surface. Because the electrostatic field direction is forward, hot electrons outside of the target are attracted to the backward direction and positive ions on the backside accelerated to the forward direction. These ions are mainly accelerated in TNSA scenario.

A portion of hot electrons with sufficiently high energy to escape intense electrostatic field at the backside do not attracted to the backward direction. These completely escaped electrons help to generate higher electrostatic field on the backside than the front side. And bulk of the target slightly becomes positive charge, which serves target expansion force with sheath field. A portion of hot electrons with sufficiently low energy to be attracted to backward direction, they return to the frontside of the target. This return electron flow is called return current. When returned hot electrons arrive in the skin depth region on the frontside, they are re-accelerated to the forward direction by the laser ponderomotive force again. These re-accelerated hot electrons become more energetic than accelerated electrons only one time, which means that frequent hot electron re-acceleration during the laser irradiation increases plasma temperature more higher value. And hot electron re-acceleration frequently happens in thin target than thick target during the same laser duration. This insight provides

thin target gets higher temperature than thick target for a same laser pulse. As the target thickness decreases, therefore, accelerated ion energy increases in TNSA regime. Moreover, hot electron
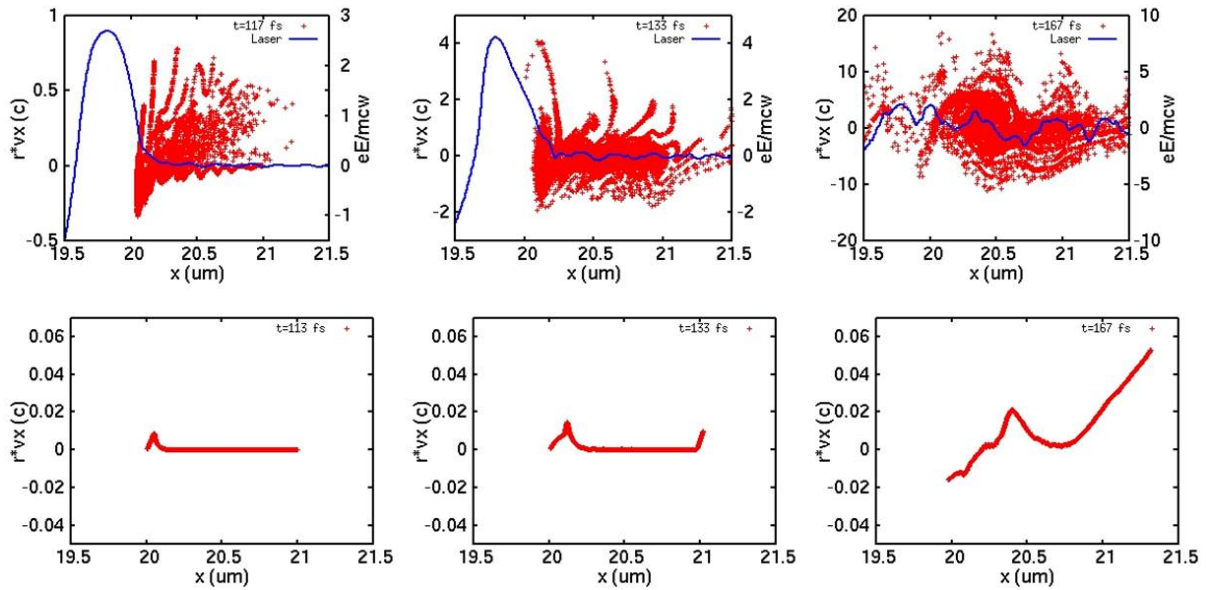
Fig. 4.1.1: 1D simulation results in TNSA regime, where linearly polarized Gaussian laser pulse with λ=1 μm, a_0=5, FWHM duration 60 fs irradiates on the plasma with n=10n_c, 1 μm thickness between 20 – 21 μm in the simulation domain. Upper low illustrates phase space of electron and laser pulse and lower low illustrates proton phase space at total simulation time t=117, 133, and 167 fs respectively.

re-circulation has an important role in electrostatic shock formation.

Accelerated hot electrons on the frontside periodically arrive on the backside due to laser ponderomotive period $\lambda/2$. Whenever hot electron bunch passes through the backside, electrostatic field increases. But whenever hot electrons return to the target inside from the outside, electrostatic field decreases. Consequently, electrostatic field intensity shows oscillating behavior in TNSA regime during the laser irradiation.

Accelerated ion energy is dependent on plasma temperature. In TNSA scenario, ions are mainly accelerated by electron sheath surrounding the bulk of plasma, which is well known as a Debye sheath. Qualitatively, as a temperature increases, much more electrons move into Debye sheath region due to high electron velocity. Therefore sheath field between bulk of plasma and electron sheath becomes stronger as a temperature increases. This sheath acceleration can be thought as sheath expansion. Mori shown plasma expansion model well describes TNSA experiments, where he well predicts cutoff energy and maximum energy of ion beam depending on the temperature.

Sheath field direction is to the normal on the surface because electron sheath surrounds entire plasma surface. In that sense, surface ions are mainly accelerated to the target normal direction at initial

acceleration stage. Wilks et al. showed that ion beam focusing using concaved target at the backside of the target regardless of Gaussian laser pulse irradiation. Many experiments have tried to measure accelerated ion beam near the target normal direction. However, sheath field direction is not always to the initial target normal direction. The direction of the field is affected by two aspects; the one is target deformation and the other is non-uniformity of the Gaussian laser pulse intensity. Hot electrons are dominantly generated on the axis of a Gaussian pulse. When they arrived on the backside, hot electron population and energy become Gaussian profile to the transverse direction during the laser irradiation. This means that sheath field has Gaussian like profile to the transverse direction at the backside. Backside ions are naturally accelerated like Gaussian shape in spatial domain during the laser irradiation, where ions on the laser axis have maximum energy. As the target structure is changed, target normal direction is also changed during the laser-target interaction. After complete laser-target interaction, sheath electrons try to shield entire plasma uniformly to remove positively charged bulk of plasma. Although sheath field directions are aligned to the plasma normal direction, the directions are different to the initial target normal direction due to target deformation like as Gaussian shape. And Gaussian like deformation shape is turned into circular like shape because of sheath expansion to the radial direction as time goes on.

4.1.2. Issue

In my experience, PIC simulations for TNSA are very tough due to thick target thickness of the order of micro meter. Simulation domain and the number of particles are huge. Furthermore, if an exact ionization dose not be implemented on the code, we can't calculate exact charge of ions and plasma density at certain position. For example, ions on the front side surface and the backside surface could be fully ionized by intense electrostatic fields but the inside of the target could not. And because of non-uniform electrostatic field intensity to the longitudinal and transverse direction, ion charge states and distribution are also different depending on their positions; the surface ions are highly ionized but the inside ions are rarely ionized. Hegelich et al reported carbon ion distribution classifying carbon charge states in experiment.

ADK-model is widely known ionization approximation. In this model, ionization potential energy for an individual charge states should be given to calculate ionization. It is problem that exact ionization potential energy is not given for atoms over the atomic number 25. It makes difficult to simulate for gold target, which has atomic number 86. Therefore, almost TNSA simulations initially load arbitrary ionized atoms without detailed discussion. In some better cases, three plasma layers are initially loaded; the front and the back side layers are composed as highly ionized ion but the inside plasma is composed as rarely ionized ions.

PIC simulation for TNSA requires initial plasma temperature in order to calculate sheath effect at initial time. If not, initial temperature is zero before the laser-plasma interaction, hydrogen layer on the front side is accelerated to the forward direction and penetrate the target in simulation; this is not true. When the initial temperature is given, hydrogen layer on the front side is accelerated to the backward direction. Of course, simulation mesh side should be smaller than the initial Debye length.
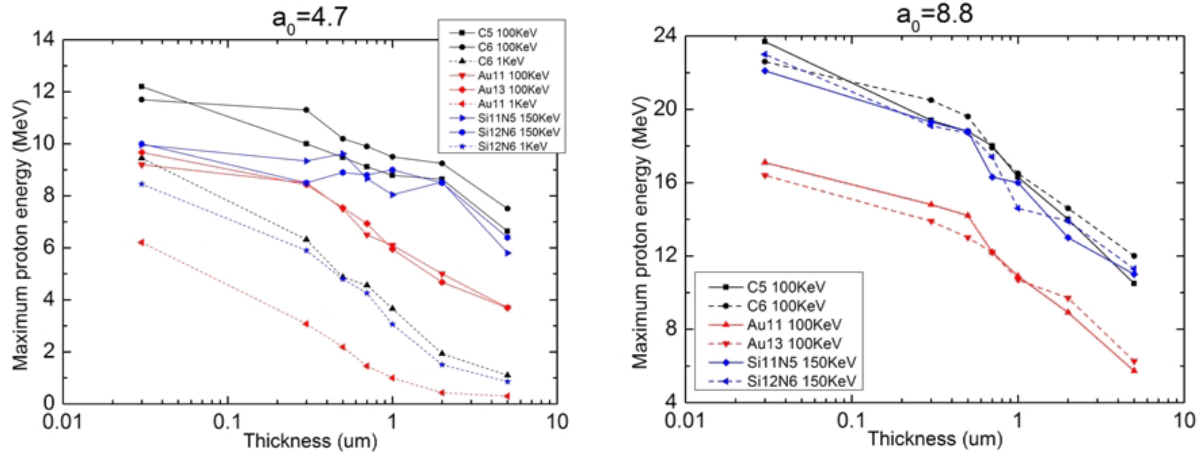
Fig. 4.1.2: One dimensional TNSA simulation using double-layer target varying thickness, species, and initial temperature. Arbitrary given initial temperature prohibits to predict simulation result.

Due to the initial temperature, plasma starts expansion before the laser irradiation. If the length between the laser launch boundary and plasma is sufficiently large, expanded plasma density profile becomes different with intended plasma density profile. Because the existence of pre-plasma increases ion beam energy in TNSA, it makes difficult to understand what affects result.

There are three methods to avoid plasma expansion by initial temperature. The first is that inserting high-order field and current calculation to suppress numerical heating. In this case plasma temperature is sustained sufficiently cold. The second is that reducing vacuum region between the laser launch boundary and plasma. The third is that loading particles with temperature just before the laser pulse arriving the plasma position. Then laser pulse irradiates the plasma before it is expanded.

Arbitrary given initial temperature prohibits ion beam energy prediction. In Fig. 4.1.2, maximum proton energy is affected by initial temperature although energy dependence on thickness is consistently observed.

Another issue is the thickness of the contamination layer. In some cases the thickness of the contamination layer is order of angstrom (10^{-10}). Then grid size becomes order of angstrom but the simulation size is still order of 10 micro meters. In order to avoid a large number of grid, the contamination layer thickness is set to the order of nano meter (10^{-9}) in simulation.

Selection of simulation finishing time should be considered in TNSA simulation. Especially in one-dimensional simulation, ions are permanently expanded by sheath field, which is very strong because

hot electrons exist only on the axis. In two-dimensional simulation, sheath field is relatively weak than one-dimensional simulation due to radially expanded sheath but it is still artifact. Although the exact simulation is three-dimensional simulation, it is very tough to run simulation. Consequently, user should finish the simulation at proper time that avoids over-estimation and under-estimation for the ion beam energy. Fuch *et al*. suggested simulation stopping time as 1.33 τ (Supplementary) [61].

4.2. Radiation pressure dominant acceleration

4.2.1. Description

A major difference between TNSA and RPDA regime is the laser polarization; linearly polarized pulse is used in TNSA but circularly polarized pulse is used in RPDA. Oscillating ponderomotive force of LP pulse periodically pushes hot electrons into plasma. But non-oscillating ponderomotive force of CP pulse cannot supply hot electrons into plasma. Non-oscillating ponderomotive force continuously piles up electrons inside plasma as an ultrathin electron layer. The thickness of the ultrathin electron layer is usually estimated as an order of skin depth for the laser pulse reflection on there. During the time, charge separation field is constructed between the remaining positive ions (electron depletion region) and ultrathin electron layer. This process is continued until the laser pressure and the charge separation field are balanced each other. Laser penetration velocity is not constant before they are balanced.

When the charge separation pressure and the laser pressure are balanced each other, electron piling process is over and the laser penetration velocity is saturated. To be concrete, if the laser intensity and plasma density are constant, the velocity of the electron layer becomes constant. Because the velocity of the ultrathin electron layer is quite slow, remaining ions in the charge depletion region are accelerated to the electrons layer and ions in the electron layer are accelerated to the forward direction by non-uniform electrostatic pressure. The former constructs a broaden ion plasma in front of the electron layer and the latter becomes main accelerated ion beam. At the same time, laser pulse continuously pushes the electron layer into the plasma that means the electrostatic pressure becomes stronger than the laser pressure due to high density of the electron layer and remaining ions. In order to balance between the charge separation pressure and the laser pressure, nearest ions trapped into the electron layer and the electron layer disperses into the plasma region. This balance and non-balance processes between two pressure make quasi-neutral electron-ion density spike and reflected ion beam like as collisionless electrostatic shock.

From now on, there are two distinct scenarios depending on the existence of the laser pulse. The one is called Hole Boring (HB), where the laser-plasma interaction is over before the quasi-neutral spike arrived on the backside of the target, and the other is called Light Sail (LS), where the laser-plasma interaction is continued after HB. Note that the LS always requires the HB before it starts. The RPDA covers HB and LS together.

After finishing the HB, the quasi-neutral density spike with constant velocity propagates into the charge neutral and cold plasma. Because the density spike passes through the entire plasma without significant interaction. The ion energy distribution in the density spike is quasi-monoenergetic. The efficiency of the HB is proportional to the $\sqrt{I}$.

21
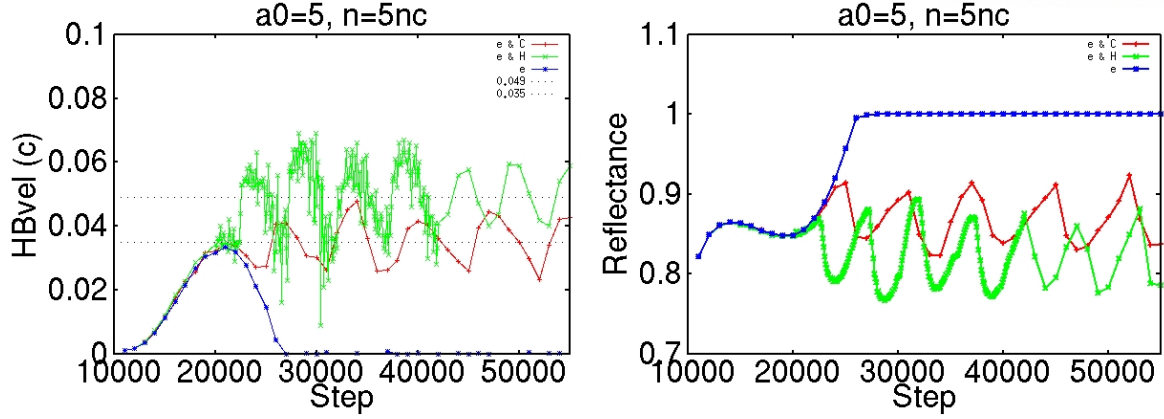
Fig. 4.2.1: HB velocity and reflectivity of 1D PIC simulation for proton (H$^+$) and carbon (C^{6+}) plasmas. Laser peak intensity is a_0=5 with 15 fs half-width-half-maximum in laser rising and falling profile and 99 fs duration at the laser peak. Averaged HB velocity and reflectance are 0.049c and 0.8185 respectively from the simulation using proton (green), which value is well agree with 0.05c from the equation. Averaged HB velocity and reflectance are 0.035c and 0.868 respectively from the simulation using carbon (red), which value is also agree with 0.036c from the equation. The blue line represents the simulation result using immobile ion, where laser front can not propagate plasma at the steady state.

The HB velocity v_{HB} can be derived from the Gauss law, charge conservation and pressure balance [28]. The exact v_{HB} is [62]

$$\frac{v_{HB}}{c} = a_0 \sqrt{\frac{1+R}{2} \frac{Z}{A} \frac{m_e}{m_p} \frac{n_c}{n_e}} \tag{23}$$

where R is reflectivity. Figure 4.2.1 illustrates HB velocity and reflectivity of 1D PIC simulation for proton (H$^+$) and carbon (C^{6+}) plasmas. Averaged HB velocity and reflectance are 0.049c and 0.8185 respectively from the simulation using proton, which value is well agree with 0.05c from the equation.

If the laser pulse duration is sufficiently long until the density spike arrived on the backside of the target, the LS starts on there. From now on, there is no charge separation field between the remained ions and the electron layer. Instead, charge displacement pressure between the electron spike and the ion spike within the quasi-neutral spike and the laser pressure are balanced each other. The laser pressure continuously accelerates the electron spike to the forward direction but the ion spike decelerates the electron spike to the backward direction; the electron spike accelerates the ion spike to the forward direction due to the law of action and reaction. Note that the quasi-neutral spike is slightly separated as the negative electron spike and the positive ion spike as long as the laser pulse irradiates on the electron spike, which can be seen in the HB process.

The laser momentum is efficiently transferred to the quasi-neutral spike in the LS process than HB process. The efficiency difference between processes could be understood through the existence of reflected ion. The reflected ion beam with two times HB velocity is generated during HB process but it is not generated during LS process. However, long pulse duration is required to reach the LS. Naturally, high total laser pulse energy is required to obtain efficient RPDA.

4.2.2. Issue

The major point to success RPDA is that compressed electron layer should be sustained as over critical density for the entire laser-plasma interaction. If the compressed electron layer is broken down under critical density, the laser pulse starts penetration and the efficient momentum transferring from the laser pulse to the compressed electron layer is finished. The more fatal point is the destruction of the density spike due to strong heating, which results in energy spreading via the sheath expansion.

In current high power laser systems, it is very difficult to get optimal target parameters, where density, thickness and density profile are contained. For a normalized laser intensity a0=5 and target density n=600n_c, HB velocity becomes $v_{HB}/c = \sqrt{Zm_e n_c/m_i n_e}\, a_0 \sim 0.003c$. The corresponding ion energy is 0.06 MeV, which is too small to adopt applications. When a_0 becomes 300 for same target parameters, ion energy is reached 230 MeV but the laser amplitude is unavailable soon.

The first RPDA experiment was done using a circularly polarized laser pulse with I=3.5-5$\times10^{19}$ W/cm^2 (a_0=3.5-5) and the target thickness in a range from 2-30 nm of the Diamond-like Carbon (600n_c for C^{6+}). In the experiment, quasi-monoenergetic ion beam was obtained. Unfortunately, no more experiment results have not been reported using higher laser intensity over a_0=5. There are two problems in RPDA experiment, the one is laser contrast ratio and the other is the normally incident condition of the laser pulse. The double plasma mirror technic is known as the outstanding method in reducing the laser contrast ratio under 10^{11}. For a peak laser intensity over I=10^{20} W/cm^2, ASE intensity is order of $I = 10^9$ W/cm^2, which is sufficiently weak to ionize the target. However laser pedestal intensity would exceed $I > 10^{12}$ W/cm^2 and the nm scale target would be ionized via tunnel ionization before the main laser pulse irradiation. As a result, pre-plasma is formed in front of the target or plasma is completely dispersed, where plasma is strongly heated during the laser pulse propagates into the under-dense plasma. The generation of hot electrons disturbs a neat density piling process during the HB. And contrast limitation in current laser system prohibits normally incident laser pulse configuration in experiment. High intensity reflected laser portion on the target could break laser system.

Non-uniform laser intensity of Gaussian pulse causes another problem in RPDA. Accelerated plasma is bent along the Gaussian profile and normal incidence condition is broken down. Then electron density decreases because electrons could be extracted by transverse electric field of the CP pulse. It

23

quickly makes compressed electron layer underdense plasma. Moreover, Gaussian laser profile itself generates non-uniform ion energy depending on the transverse position. As a position of ion is far from the pulse axis, generated ion energy is reduced. A super-Gaussian laser pulse has been suggested to avoid non-uniformity of Gaussian pulse.

4.3. Collisionless electrostatic shock ion acceleration

4.3.1. Description

Conceptually, the shock is the propagation of a physical discontinuity with higher velocity than the sound speed of a medium. The easiest concept of a physical discontinuity is the density jump like as a step function. When the high density region expands to the low density region with higher velocity than the sound speed, this can be regarded as the shock. There is a variety of shock depending on conditions. Among them, collisionless electrostatic shock (CES) is mainly utilized to accelerate ion in laser-plasma acceleration.

The collisionless electrostatic shock (CES) means that the shock moves with electrostatic field together. Unlike the acoustic shock in air, CES can be generated only in plasma because charged particles are required to form the electrostatic field. A neighboring charged particle is influenced by the electrostatic field of the shock with velocity v_{sh}. A stationary positive ion will be face with the shock front and then the ion is reflected to the forward direction by the electrostatic field on the shock. Because this process is collisionless, the reflected ion has a velocity $v \sim 2v_{sh}$ like as elastic collision. A major interest in CES ion acceleration is on the reflected ion beam which has high energy and quasi-monoenergetic spectrum.

The important condition to form CES, the Mach Number $M=v/c_s$ should be in a range $1.5 < M < 3.7$, where $c_s = (ZKT_e/M)^{0.5}$ is the plasma sound speed, Z is the ion charge state, T_e is the upstream electron temperature, M is the ion mass. Therefore, there are three aims to generate CES in laser-plasma interaction; the one is generation of density discontinuity, the second is the acceleration of the density discontinuity, the third is plasma heating in upstream to satisfy the Mach number condition.

The one and second aims are established by a reflection of the laser pulse on the plasma, where the laser pulse compresses the plasma by transferring its momentum. The upstream heating is compensated by the hot electron re-circulation by the oscillating ponderomotive force of a linearly polarized laser pulse.

Chapter V

Control of the charge and energy of the proton beams from a laser-driven double-layer target

5.1 Introduction

Ion acceleration from an ultraintense laser pulse and a thin target has attracted much interest as a potential ion beam source with compactness and low cost compared to conventional technologies. Depending on the power regime of the driving laser pulse, numerous scenarios of ion acceleration have been suggested and tested by theory, simulations, and experiments [56]. Among them the target normal sheath acceleration (TNSA) [21-25, 63] has a relatively long history, and is still gaining much interest, since it can be realized even with a moderate laser power.

Though the TNSA has an intrinsic disadvantage in the broad energy spectrum of the accelerated heavy ions, the acceleration of light ions like protons still has some benefits from the TNSA mechanism by employing a double-layer target [64-72]. In this scheme a thin proton layer coated on the main target is accelerated as a single body by the sheath field, yielding a quasi-monoenergetic proton beam. Due to its natural abundance in the form of a contamination layer [21], some attentions have been paid to the double-layer scheme. For instance, Esirkepov *et al*. [69] studied the scaling of proton energy by varying the laser intensity for the different areal densities of the target. Yu *et al*. [70, 71] investigated the effects of the layer thickness, where they found that the maximum proton energy increased as the layer thickness increased up to a certain level. Somewhat differently, Robinson *et al*. [72] analytically studied the influence of the areal density of the proton-ion composite (mixture) target on the proton energy spectrum. However, the combined effects of the substrate thickness and the areal density of the proton layer have not been systematically studied previously.

Recently the technique of the self-assembly monolayers (SAMs) [73] has become available, enabling a separate control of both the layer density and thickness. On the other hand, it is well known that the sheath field from the main target increases as the target thickness is reduced down to roughly the skin depth [38, 69]. Motivated by these, we naturally suggest a separate control of the proton beam charge by the layer's areal density as well as the beam energy by the main target (called a substrate from here on) thickness. We studied this idea for the first time by a series of one-dimensional particle-in-cell (PIC) simulations to eventually find that those two control parameters, i.e. the areal density $\sigma=nl$ of the proton layer and the substrate thickness L, do not interfere strongly. This conclusion indicates that σ and L can be utilized as design parameters of the beam charge and energy in the double layer scheme.

This chapter is organized as follows. In Section 5.2, the simulation conditions are described. In Section 5.3, the effects of the areal density of the layer are briefly reviewed along with our own

simulation results. The effects of the substrate thickness can be found in Section 5.4, followed by a summary.

5.2 Simulation set up

For the simulations, we used a one-dimensional particle-in-cell (PIC) code, where a numerical-dispersion-free field solver in a propagation direction was employed [74], and the third order current calculation and the field interpolation were used to reduce the numerical noise for the high density plasmas.
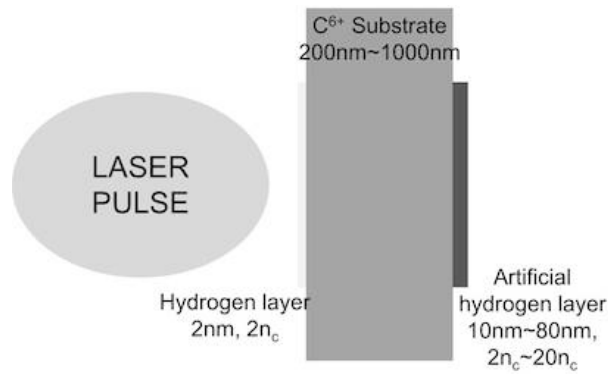
Fig. 5.1: The target configuration. We varied the thickness and density of the artificial hydrogen layer on the backside from 10 nm to 80 nm, and from $4n_c$ to $20n_c$, respectively. The substrate was varied from 200 nm to 1000 nm in thickness with a fixed density $600n_c$. Another hydrogen layer with 2 nm in thickness and $2n_c$ density was on the front side of the substrate, assuming hydrogen contamination.

The physical parameters were set as realistically as possible: for the substrate, we assumed fully ionized C^{6+} and electron plasma with the density $600n_c$. A thin proton layer, whose thickness and density were 2 nm and $2n_c$, respectively, was put on the front side of the target, corresponding to a contamination layer. On the back side, an artificial proton layer was assumed to be coated with variable thicknesses from 10 to 80 nm, and densities from 2 to $20n_c$. The target configuration is presented in Fig. 5.1. The driving laser pulse was linearly polarized and longitudinally Gaussian with the normalized vector potential $a_0=10$, where $a_0=eE/mc\omega$, e and m are the charge and mass of an electron, respectively, E and ω are the electric field and angular frequency of the laser pulse, respectively, and c is the speed of light}. The wavelength and the pulse duration were 1 μm and 27 fs in FWHM, respectively. The length of the simulation domain was 20 μm with the mesh size 0.5 nm, which was sufficiently small enough to resolve the initial proton layer thickness and the Debye length. The number of macro particles per species per cell was 1000. The initial electron temperatures of the front side proton layer, main target, and the back side proton layer were set as 100 eV, 10 keV, and

500 eV, respectively, to start the simulation with the Debye length resolved by the mesh. The different initial temperature of each layer used in our simulations does not influence significantly the calculation, since the target temperature increases very rapidly up to MeV as soon as the laser pulse irradiates the target. Pre-plasmas were not considered assuming a high contrast ratio of the driving pulse.

Usually in one-dimensional simulations, the accelerating field tends to be sustained permanently in the TNSA regime, since the sheath field expansion in the radial direction on the back side cannot be properly counted. In order to avoid the overestimation of the proton energy by such an artefact, the simulation should be stopped at a certain point. Among various criteria for the simulation stop, a formula by Fuchs *et al.* [61], where the sheath expansion is taken into account, is known to be consistent with numerous simulations and experiments for a short driving laser pulse, as in our work. The formula is described by $t_{acc} = \alpha(\tau_L + t_{min})$, where t_{acc} is the acceleration time in the rear-surface, t_{min} an empirical constant defined by 60 fs, τ_L is the laser pulse duration, and α is another empirical constant, whose value is 1.3 for a laser intensity higher than 3×10^{19} W/cm^2. Then the corresponding acceleration time is t_{acc} = 134 fs for our simulation condition. Considering the time taken by the pulse to arrive at the front side, we stopped the simulations after 153–156 fs, depending on the target thickness.

5.3 Effects of the areal density of the proton layer

The average and maximum energy of the proton beams from the layer are known to be dependent on the initial areal density σ [66, 69, 70], which is the product of layer density n and the thickness *l*. We verified by a series of simulations that such a previous conclusion is valid for quite a broad range of the layer parameters, including the case where the thickness or the density is comparable to those of the sheath.

We conducted a series of simulations for quite a broad range of the layer parameters, including the case where the thickness or the density is comparable to those of the sheath.

This point is immediately noticed from the left column of Fig. 5.2. For different substrate thicknesses, the colored strips, which correspond to constant-energy contours, coincide well with the line of constant areal densities, decreasing overall as σ increases. Here, the simulations were carried out for the layer thicknesses ranging from 10 nm to 80 nm, and the densities from $2n_c$ to $20n_c$. Note that the average length and the electron density of the sheath were measured to be a few tens of nano-meters and several tens of the critical density, which were comparable to the maxim density and thickness of the layer.

Opposite to the average energy, the maximum energy of the protons increases as σ increases due to the influence of the Coulomb repulsion between the protons. In this case also, the maximum proton
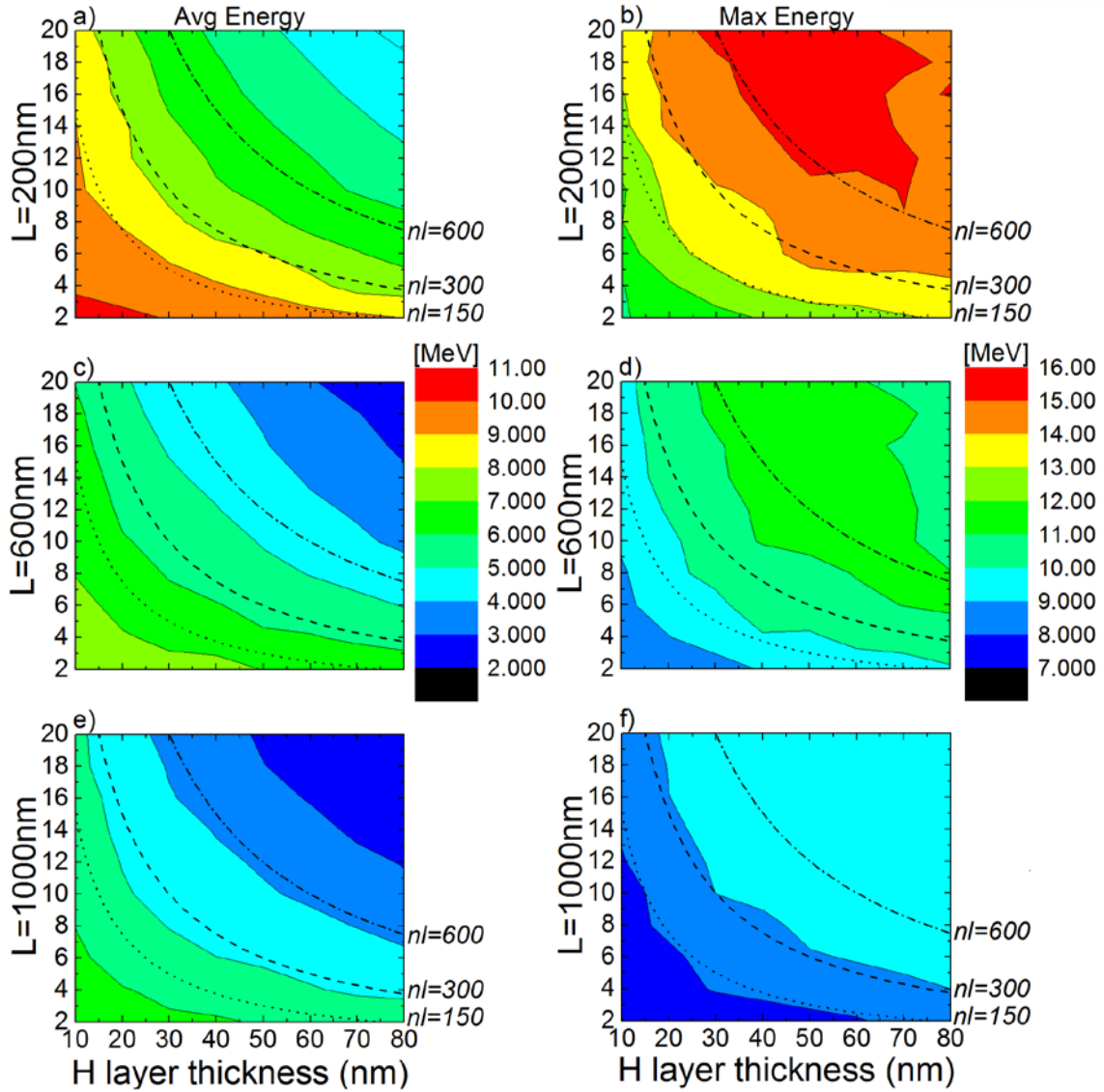
Fig. 5.2: Contour plots of the average (left column) and the maximum (right column) energies of protons vs. the thickness and density of the hydrogen layer for different substrate thickness.

energy is dominantly determined by the areal density as in the right column of Fig. 5.2. This result can be explained by considering the maximum electric field at the proton beam edge, represented [70, 71]

$$E_{\max}\left(\frac{l}{2},t\right) = E_s \pm \frac{2\pi enl}{1+2\pi ne^2t^2/m_p} \tag{24}$$

where l is the proton beam thickness, E_s the sheath field, and m_p the proton mass, respectively. Note that the maximum field described by the above equation depends on the product of n and l, i.e. σ. Since the maximally energetic protons come from the layer edge, whose part is most strongly accelerated by this maximum field, consequently the maximum proton energy should be determined by the areal density.

5.4 Effects of the substrate thickness

The virtue of manipulating the areal density of the proton layer is that the proton beam charge can be put under control; the total beam charge is the same as the initial proton charge in the layer, since the detached proton layer is accelerated as a whole. However the beam charge increment comes at the cost of the decreased average beam energy. Though the maximum proton energy usually increases for a higher areal density by the Coulomb repulsion, in this case, the energy spectrum becomes wider.

One way to preserve or increase the average proton energy even with an increased beam charge is to enhance the sheath field formed by the substrate electron. Fortunately, it is possible to find evidences indicating the sheath field is enhanced as the substrate is thinned [38]. As the substrate thickness L is reduced, the hot electron re-circulation happens more frequently, building up in the sheath region, and eventually leading to the enhancement of the field energy of the sheath [75]. Figure 5.3 illustrates well the sheath field depending on the substrate thickness. In Fig. 5.3(a), it is shown that the sheath field strength and the sheath length measured at each temporal peak increases as the substrate thickness is reduced. The inset of Fig. 5.3(b) represents the number of electrons gathering in the backside of the substrate. The oscillation behavior is due to the hot electrons periodically supplied by the oscillating ponderomotive force with $\lambda/2c$ of the laser pulse. Figure 5.3(b) is the second order polynomial fitting of the inset figure, which shows that as the substrate thickness is reduced, more abundant electrons gather in the sheath region. Such an increment of the sheath field is expected to be continued until L reaches the skin depth of the plasma [38].
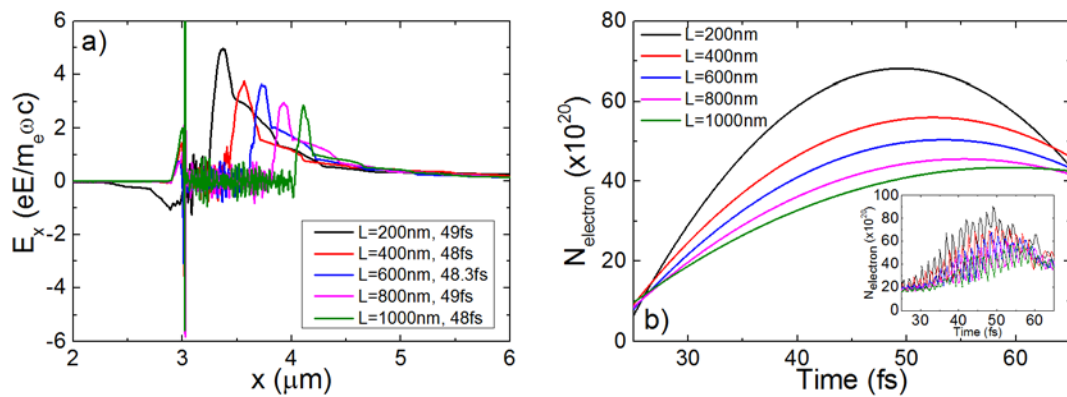
Fig. 5.3: (a) Longitudinal fields for different substrate thicknesses, for l=10 nm, n=2n_c, during the laser-target interaction (48 fs). (b) The number of electrons in the backside of the substrate during the laser-target interaction. The curved lines are the second order polynomial fitting of the inset figure which illustrates the oscillation behavior of the number of electrons outside of the substrate.
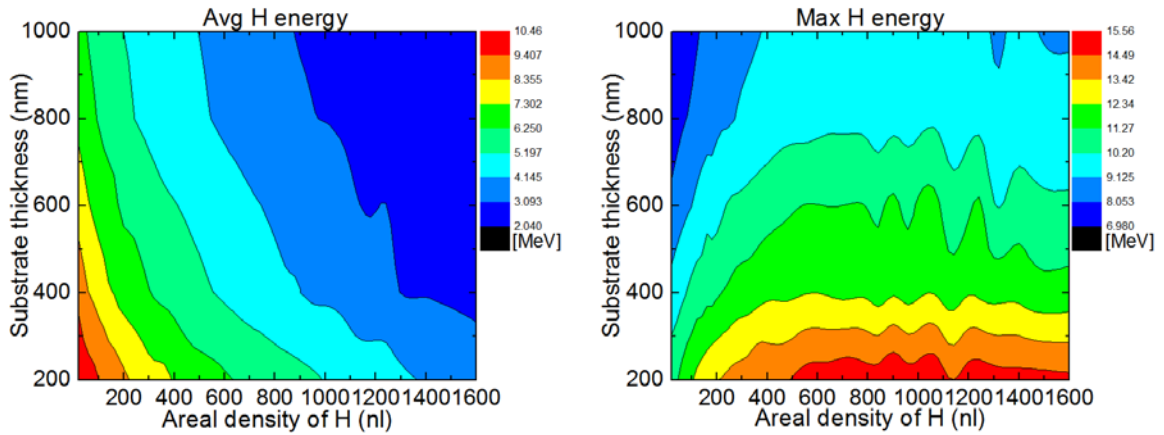
Fig. 5.4: Contour plots of (a) the average and (b) the maximum energy vs. areal density and substrate thickness.

In the meantime, the hot electron temperature is not influenced by the proton layer on the back side of the substrate, since the hot electrons in the sheath are generated on the front side of the substrate, and its temperature is determined by the laser pulse intensity [76], polarization [30] and pre-plasma state [77]. Therefore, for a fixed laser condition with a high contrast ratio as in our case, the substrate thickness and the areal density of the proton layer can be regarded as independent control parameters of the total proton charge and beam energy.

Such an expectation could be confirmed from a series of one-dimensional PIC simulations, as presented in Fig. 5.4 (a). From this figure it is apparent that the average proton energy decreases as the areal density of the layer increases (along the abscissa), while a higher proton energy is obtainable by reducing the substrate thickness (along the ordinate). In our simulations, the highest average energy of the proton beams was measured to be more than 10 MeV for a 200 nm-thick substrate.

Figure 5.4 (b) exhibits even more interesting results: the maximum energy of the proton beam is more strongly dependent on the substrate thickness than on the areal density. This point is implied by the almost horizontally lying color strips for roughly $\sigma > 600$. For a lower areal density than that, the maximum proton energy is influenced both by the substrate thickness and the areal density itself. The origin of the oscillation-like pattern in the maximum energy of the proton in the high-areal-density region in Fig. 5.4 (b) is not clear.

In Fig. 5.5, we examined the fractional spectral width $(\varepsilon_{max} - \varepsilon_{min})/\varepsilon_{avg}$ of the proton beams depending on the substrate thickness and the areal density of the layer, where ε_{max}, ε_{min} and ε_{avg} are the maximum, minimum and average proton beam energy respectively. As expected in Ref. [72], the energy spread of the proton beams is strongly dependent on σ. However it is found from this figure that the substrate

31

thickness does not influence much on the energy spectrum, especially for the quasi-monoenergetic proton beam with narrow spectral width under < 0.2; the value 0.2 is empirically accepted as 'quasi-
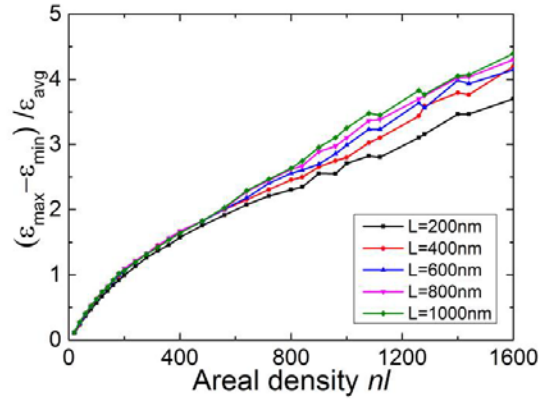
Fig. 5.5: Fractional spectral width $(\varepsilon_{max} - \varepsilon_{min})/\varepsilon_{avg}$ of the proton beam vs. the areal density of the layer for different substrate thicknesses. The smaller the specral width is, the more quasi-monoenergetic of the proton beam is.

monoenergetic in former literatures like Ref. [26, 27].

As a consequence, the results presented in this section indicate that the effects of the substrate thickness and the areal density of the layer do not interfere strongly with each other. Therefore the beam energy can be controlled separately by the substrate thickness, while the beam charge and the spectrum width can be controlled by the areal density.

5.5 Conclusion

We studied control of the charge and energy of proton beams accelerated from a laser-driven double-layer target. From a series of one-dimensional PIC simulations, we could confirm that the decrease in the average beam energy resulting from increasing the layer's areal density can be compensated for by reducing the substrate thickness is building up more electrons in the sheath region as the re-circulation period is reduced, eventually leading to an enhanced sheath field. Most importantly we discovered that two control parameters, i.e. the areal density of the hydrogen layer, and the substrate thickness, do not interfere with each other significantly. Furthermore, the maximum energy of the protons, which are influenced by the repulsive Coulomb force, can actually be controlled more dominantly by the substrate thickness. In the case of spectrum width, the influence of the substrate thickness was found to be small in the mono-energetic regime.

Since the substrate thickness can be readily changed experimentally, and the areal density of the hydrogen layer can also be manipulated by resorting to a modern SAM technique, we suggest those two factors as feasible control parameters of the beam charge, spectrum width, and average or

maximum energy of the protons from a laser-driven double-layer TNSA scheme. Though our study is based on one-dimensional simulations, it may represent still well the underlying physics related with substrate thickness and the areal density of the proton layer, especially when the proton layer patch is smaller than the pulse spot size.

• This section is the result of the printed paper at Phys. Rev. E **92,** 043102 (2015).

Chapter VI

Shock ion acceleration by an ultrashort circularly polarized laser pulse via relativistic transparency in an exploded target

6.1 Introduction

The methods to generate MeV-class ion beams from interaction of intense laser and thin targets are attracting widespread interest from cancer therapy, material engineering [78, 79], and proton imaging. Those applications usually require the ion beams to be as monoenergetic as possible, in order to get a concentrated dose on the cancer cells or high-contrast imaging. For quasimonoenergetic ion beams from laser-target interaction, the technique of target-normal-sheath-acceleration (TNSA) combined with the second layer of light species is available with a practical laser intensity such as $I<10^{21}$ W/cm^2 [80]. Another scheme is radiation pressure acceleration (RPA), where the light pressure pushes an ultrathin ion layer continuously as a single quiasimonoenergetic bunch in the light-sail regime. However, the energy conversion efficiency is usually very low in TNSA. On the other hand, an ultrahigh contrast ratio more than 10^{-11} of the driving pulse is required in RPA. Furthermore RPA very demands pulse intensity beyond the feasible range of small-room-scale laser systems.

Recently it was suggested to use an electrostatic shock [45, 62, 81-86] for ion acceleration, where a laser pulse with moderate power and a near-critical target are used. In this system, a stable electrostatic shock with a high Mach number (M>1.5) is formed in a similar way as in Ref. [87]. As the shock is a highly positive, propagating ion density spike, a quasimonoenergetic ion beam can be generated through the reflection of incoming ions on the shock front. One essential condition for the shock formation is warm electrons [87], which is achieved via the recirculation of hot electrons generated by the oscillating ponderomotive force of the driving pulse. Simultaneously the driving pulse makes an initial density spike of plasma moving with a piston velocity [62]. Another condition for the shock formation is that the piston velocity of the spike be large enough to match the shock velocity. To meet this condition, the target density should be suitably low (<100 n_c) [45], which can be achieved by using a long wavelength (10 μm) CO_2 laser, along with a high-density gas instead of a solid target [85, 88].

In this chapter, we discovered another route to shock formation and related ion acceleration by a laser pulse with short wavelength (~1 μm), moderate peak power (1.1-1.4 PW) and energy (28-42 J), ultrashort duration (20-40 fs), and circular polarization. To meet the low-density condition of the plasma, we employed an exploded target [89-91], where the plasma ionized primarily by the ASE or prepulse expands and its density decreases until the main pulse arrives. What we discovered is that the electron heating by relativistic transparency (RT) can be an essential step for shock formation. This is

contrasted to the conventional way of heating via an oscillating ponderomotive force of a linearly polarized wave and subsequent recirculation of the energetic electrons [45, 62, 81-86]. In the meantime, the reflected portion of the pulse energy contributes to the initial pistoning of an ion density spike. The penetrating electromagnetic field heats the electrons rapidly compared to the electron recirculation process, allowing the use of an ultrashort pulse of several tens of femtoseconds. On the other hand the circular polarized pulse can piston the initial density spike to the required Mach number faster than the linear one with the same energy. Consequently the circularly polarized pulse can be more efficient than the linear one in shock ion acceleration under the limited pulse energy. In our scheme, controlled pre-pulse energy and duration are utilized for target explosion [86].

This chapter is organized as follows. An RT-based shock acceleration is shown through one-dimensional simulations in Sec. 6.2. A three-dimensional simulation is presented in Sec. 6.3. The conclusion is given in Sec. 6.4.

6.2 One-dimensional simulations

From one-dimensional particle-in-cell (PIC) simulations, we observed that direct electron heating by the laser penetration developed a Mach number lager than 1.5, resulting in high shock velocity (~0.2c), using a 1.4 PW, 20 fs laser pulse. The shock formation and ion acceleration could also be observed in full three-dimensional PIC simulations with slightly different laser and plasma parameters.

For the one-dimensional PIC simulations using a verified code [93-95], a circularly polarized Gaussian laser pulse with $\lambda = 1$ μm, τ (pulse duration) = 20 fs, and a_0 (normalized vector potential) = 18 was launched from the left side of the simulation box, which was 40 μm long, divided by 1 nm meshes. To model the density profile of the initially rectangular, vacuum-expanding plasma, we adopted a formula obtained from the hydrocalculation in Ref. [89]:

$$n_i(x) = \frac{2n_{i,\max}}{1 + \exp\left[\dfrac{2\nu\theta(\nu)}{l_r} - \dfrac{2\nu\theta(-\nu)}{l_f}\right]} \tag{25}$$

Where $\nu = x - 0.5l_0$ and $\theta(x)$ is the step function. The parameters n_i, $n_{i,\max}$, l_f, l_r and l_0 are the plasma density, the maximum plasma density, the front and backside scale lengths of the density, and the initial target thickness, respectively For a target with l_0=30 nm and n_0=600n_c located at X=20 μm, we conducted the simulations with three different levels of expansion with $l_f = l_r$ =1, 2, and 3 μm. Corresponding peak densities were $n_{e,\max}$=13, 6.5, and 4.3n_c, respectively, from integration of Eq. (25) $\left[\int n_i\, dx = n_0 l_0 / (l_{fr} + l_r) / \ln 2\right]$. We assumed fully ionized carbon plasma (C^{6+}). The number of particles per cell per species was 200 at the maximum density, which was sufficiently large to suppress numerical heating and to represent the tail part of the plasma density with a large enough number of macro particles.
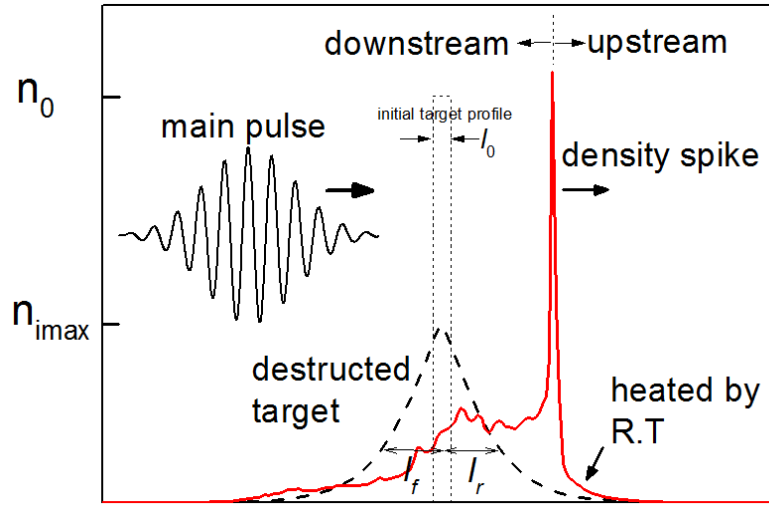
Fig. 6.1: Schematic of initial simulation setup and shock profile after interaction. Original solid target with initial density n_0 and thickness l_0 is destructed by ASE into exponential like profile with scale length l_f, l_r and maximum density n_{imax}.

Figure 6.2 is the representative one-dimensional result, illustrating the new procedure of shock formation well. The left column exhibits three steps of shock formation: (a) density spike formed by the ponderomotive force of the circularly polarized pulse, (b) partial transparency of the pulse energy by the relativistic effect and related electron heating, and (c) shock formation after leaving of the transparent pulse and ion acceleration. In step (a), the velocity of the density spike moves with a piston velocity, which is comparable to the shock velocity, which appears later, but it is not a shock yet: the charge is almost neutral, which indicates that it is just a compressed bunch of ions and electrons. The evidences for the RT-induced electron heating in step (b) can be found from Fig. 2 (d). For $l_f = 2$ and $3~\mu$m, where the target densities are low enough to induce RT, the electron temperature in the upstream increases significantly up to several MeV. The temperature increment begins from $t = 120$ fs, which is coincident with the start of RT [Fig. 2(a)]. Meanwhile the electron temperature remains noticeably cold at around 400 keV for $l_f = 1~\mu$m, where the target density is too high to induce RT. In our simulations, the electron density in the density spike for $l_f = 2$ and $3~\mu$m was lower than the RT threshold approximately given by $\sqrt{1+a_0^2}\,n_c \approx 18 n_c$, while it was not for $l_f = 1~\mu$m. Such a heating mechanism by the relativistic transparency is different from that of previous works in Refs. [45, 62, 81-86], where the electron recirculation by the reflection from the sheath field dominates. Note that step (c) occurs only after complete leaving of the pulse, indicating the shock is electrostatic. This is a different feature from that of Yin *et al*. [92], where an electromagnetic solitary wave is generated during the interaction between the laser field and plasma.
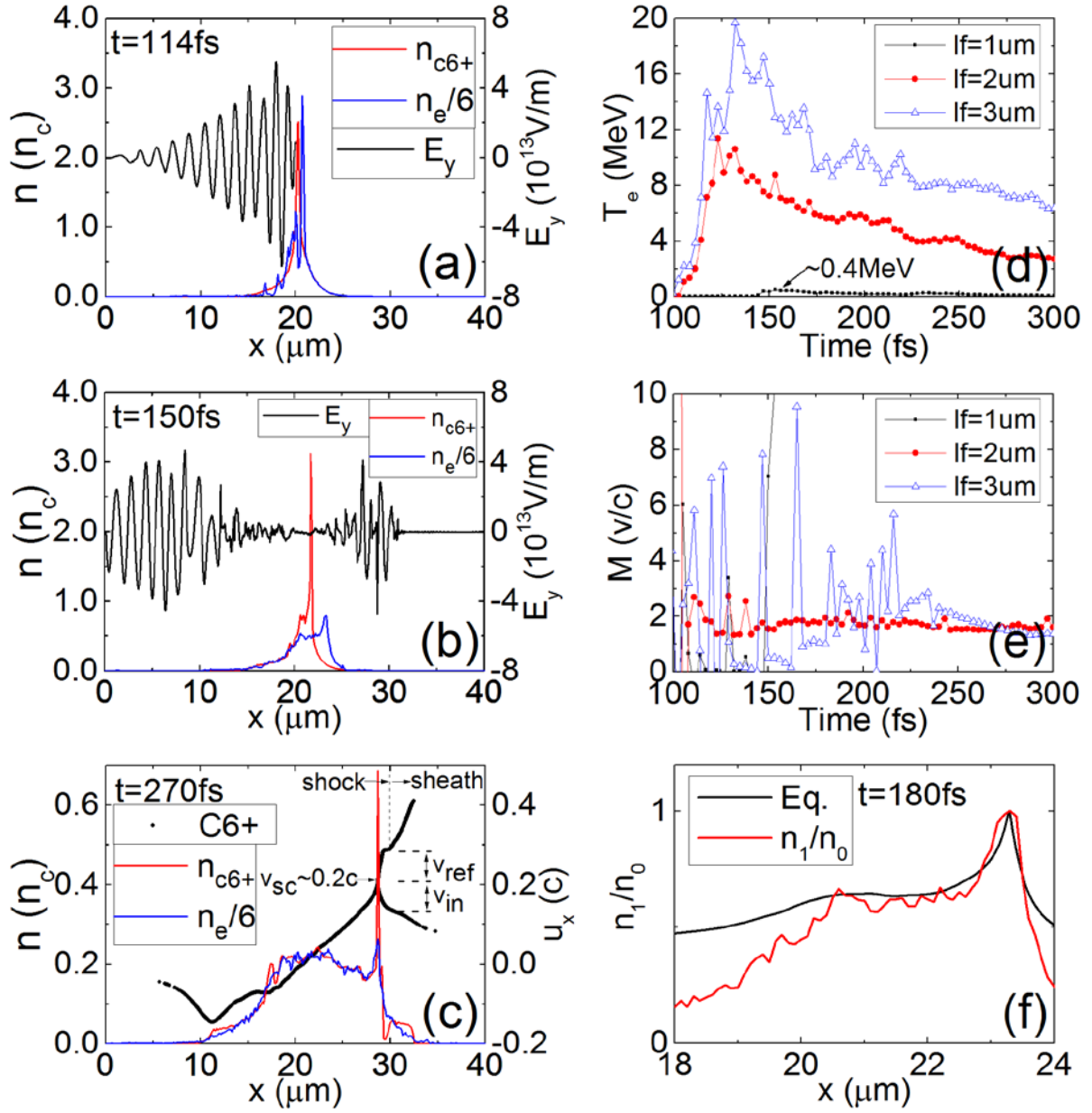
Fig. 6.2: One dimensional simulations with $a_0=18$, circular polarization, and pulse duration 20 fs. $l_f = 2$ μm for (a)-(c) and (f). (a) Compression of initial density spike, (b) during RT, and (c) after RT along with the ion phase space. (d) Average electron temperature in the upstream for different l_f and (e) Mach numbers. (f) Comparison of Eq. (2) and simulation data for $l_f = 2$ μm.

The existence of the shock could also be qualitatively verified from the measurement of Mach number of the density spike and velocity doubling of incident ions in the phase space. Figure 1 (e) represents the Mach numbers of the density spikes for three different cases ($l_f = 1, 2, 3$ μm). From Ref. [87], the Mach number of the laminar electrostatic shock should be $1.5 < M < 3.7$, which is satisfied

by the $l_f = 2$ μm case (M ~ 1.6). The velocity doubling by the reflection of incident ions can also be found in Fig. 6.2 (c). As the shock collects ions in front of it via reflection, a distinct characteristics of shock acceleration could not be observed in the cases with $l_f = 1$ or 3 μm.

In order to demonstrate more rigorously that the density spike in Fig. 6.2 is actually a laminar electrostatic shock, we compared the density profile from the simulation with the following equation suggested by Forslund *et al*. [87], which relates the electron density and potential difference in the downstream:

$$\frac{n_1}{n_0} = \frac{2\psi}{\sqrt{\pi}} + e^{\psi}\,\mathrm{erfc}\left(\sqrt{\psi}\right) \qquad (26)$$

where $\psi = e\varphi / kT_e$, φ is the potential, T_e is the upstream electron temperature, n_1 is the downstream density, and erfc(x) is the complement error function. As can be seen from Fig. 6.2 (f), this equation coincides well with the density in the downstream from $X = 20.5$ to 23.5 μm measured from the simulation with $l_f = 2$ μm. We could not find any good match between Eq. (26) and the simulation results for $l_f = 1$ and 3 μm, implying they are not actually shocks.

One interesting aspect of the exploded target is that the created shock can be sustained for a long time in the decreasing plasma density even in the absence of the laser pressure. For the exploded target, which has an exponentially decreasing density profile in the backside, the number of incident ions on the shock front is considerably reduced compared to the uniform case. Hence, the shock structure can propagate in the plasma without significant momentum loss, which enables it to sustain the shock even without the driving laser pulse. For $l_f = 2$ μm, it is found that the shock velocity is reduced just slightly even after complete leaving of the laser field at t=200 fs. The final shock velocity is about 0.2c, which does not deviate significantly from the initial piston velocity. On the other hand, in the $l_f = 1$ μm case, the velocity of the ion density spike is constant at 0.17c throughout the simulation, which indicates that there is no momentum transfer at all from the spike to the background ions. In this case, abundant cold electrons quickly shield the reflecting field from the ion density spike, which is generated in the early hole-boring stage, and they just ballistically propagate without the driving laser pressure.

l_f (μm)	γ	E_k (MeV)	$\Delta\varphi$ (MeV)	$\Delta\varphi - E_k$
1	1.1	0.05	2	+
2	20	10	20	+
3	60	30	15	-

TABLE 6.1. Average gamma factor of electrons, average electron kinetic energy E_k near the ion density peak, and potential difference from the ion density peak to 1.5 μm away from that, at t = 180 fs. In the case of $l_f = 3$ μm, $\Delta\varphi - E_k < 0$.

Extremely high electron temperatures can prohibit the shock formation (the case of $l_f = 3$ μm). Highly energetic electrons easily escape the shock potential, showing an oscillating behavior [62]. Accordingly the electrostatic field also oscillates, which eventually smears out the density spike of the shock. Approximately $q\varphi > 0.5\gamma m_e v_e^2$ is one of the necessary conditions for stable shock formation. To check this from out simulations, we measured the potential difference and the average kinetic energy of electrons over the position between the density peak and 1.5 μm away from that, which was sufficiently wide to cover the Debye length around the density spike. These measurements are summarized in Table 6.1. For $l_f = 3$ μm, where the relativistic transparency is strongest and the temperature is two times higher than that for the $l_f = 2$ μm case, the electron's kinetic energy is higher than the potential energy, ending up with smeared-out shock eventually.
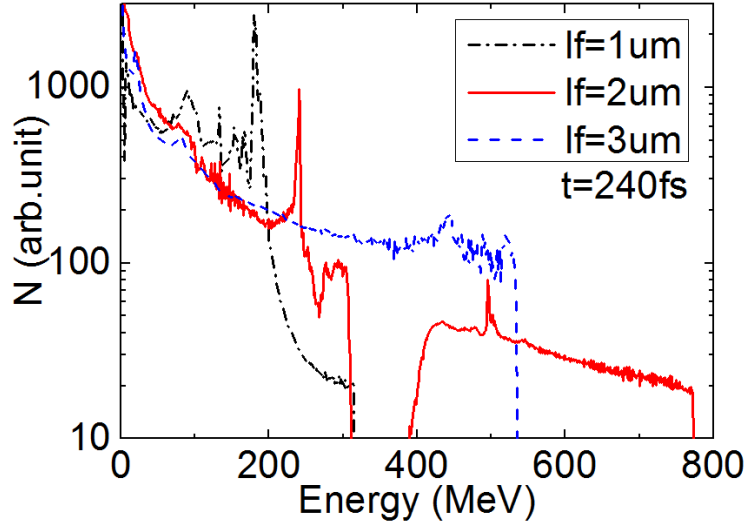
Fig. 6.3: Energy spectra of the accelerated ion beams for three different cases: $l_f = 1$, 2, and 3 μm at t = 240 fs.

From Fig. 6.3, it is clear that the $l_f = 2$ μm case yielded the best ion beam acceleration among three exploded targets. An ion beam over 400 MeV, originating from the reflected ions on the shock front, is well separated from the thermal beam under 300 MeV. The latter is from the shock itself and the downstream ions. Due to the combination of the shock and sheath acceleration, $l_f = 2$ μm plasma generated the highest maximum ion energy at 780 MeV. Another interesting feature is that the shock itself contains a quiasimonoenergetic peak at 240 MeV, which is relatively high compared with 180 MeV from the RPT-dominant case with $l_f = 1$ μm. When the transparency of the laser pulse was too high ($l_f = 3$ μm), the high electron temperature led to a thermal energy spectrum of the ion beam.
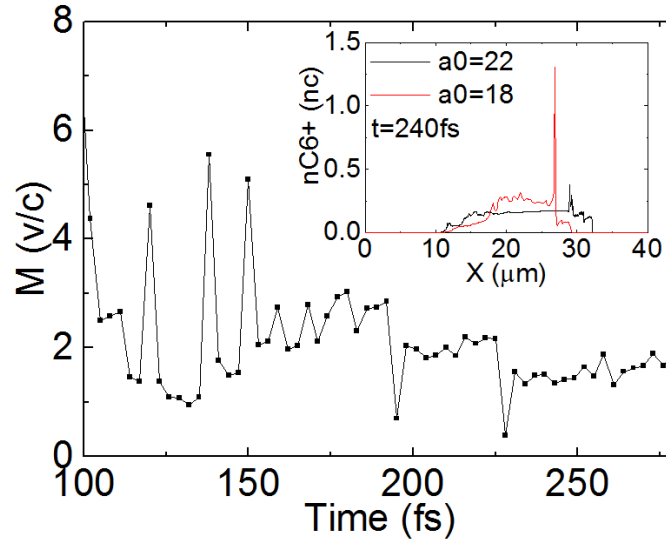
Fig. 6.4: Mach number oscillation ofr increased laser intensity from a_0 = 18 to 22 for l_f = 2 μm. Inset represents the density spikes for a_0 = 22 (dotted black line) and 18 (solid red line).

When the laser pulse intensity increase from a_0 = 22 keeping other parameters the same as in the l_f = 2 μm case, the RT effect increases to yield a similar oscillating behavior of Mach number (see Fig. 6.4) as in the previous l_f = 3 μm case with a_0 = 18. In this case, the shock diminishes quickly even for a higher driving power (see the inset). On the other hand, when the laser pulse intensity decreases from a_0 = 18 to a_0 = 10 the shock acceleration turns into RPA dominant process (not shown here).

When the same ultrashort laser pulse is linearly polarized, no meaningful density spike could be observed in out supplemental simulations for a_0 = 10-25.5. Usually such a longer pulse is required in the linearly polarized case so as to push the density spike deep into the higher-density target. However, under the same total pulse energy, the peak intensity of the pulse should be decreased as the pulse duration is prolonged, which may yield much decreased ion energy. When the pulse duration is prolonged to 1 ps under our simulation conditions, a_0 becomes 2.5. From the scaling law of the ion energy presented in Ref. [45], the optimized carbon ion energy driven by a linearly polarized pulse is less than 100 MeV, which is significantly smaller than that in Fig. 2. Furthermore, the reduction of the target density should be accompanied to the lowered a_0, which will inevitably decrease the accelerated beam charge.
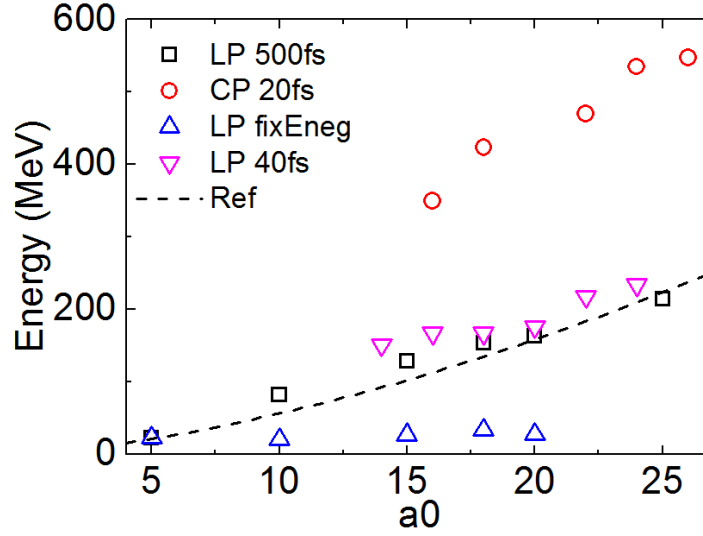
Fig. 6.5: Scaling of ion (C^{6+}) energy as a function of laser amplitude, obtained from one-dimensional PIC simulations. Four different cases are presented; circularly polarized (CP) pulses with $\tau = 20$ fs and $l_f = 2$ μm (circles), where τ is the pulse duration. They can be directly compared with the linearly polarized (LP) pulses with $\tau = 40$ fs and $l_f = 2$ μm (inverted triangles). LP pulses with $\tau = 500$ fs and expoenetial plasma tail in the rear side with $l_f = 2$ μm (squares). LP pulses with varying a_0 and τ, keeping the pulse energy ($\sim a_0\tau$) constant by that of $a_0 = 18$ and $\tau = 20$ fs case of CP, and with $l_f = 20$ μm (triangles). Dashed line represents the ion energy scaling law from Ref. [45] for $\tau = 500$ fs, C^{6+} ion, and $l_f = 20$ μm.

It is found from Fig. 6.5 that the RT-based shock is quite robust for a broad range of laser and target parameters. In his figure, one-dimensional PIC simulations for the ion energy versus the amplitude a_0 of the driver pulse are presented. In each case the target parameters are arranged so that the shock is formed properly. The higher the ion energy is for the stronger laser intensity, as the hole-boring speed and accordingly the shock velocity increases. In addition, a comparison with the cases from linearly polarized (LP) pulses with the same pulse energy is presented. In LP cases, usually a higher plasma density is required to compress the density spike by preventing the transparency. Thus the HB velocity is slower in LP cases, leading to lower ion energies (but obviously a higher beam charge from the high-density plasma). Note that the LP cases follow well the scaling law from Ref. [45], denoted by a dashed line in the figure.

Throughout our simulations, we used 1 μm for the wavelength of the driver laser pulse. A more practical wavelength of the short laser pulse may be at around 800 nm from a Ti:sapphire laser system. The relativistic transparency, which is suggested as one of the major steps for the shock formation, is determined dominantly by the electron density. Hence we expect a slight scaling up of the target

density and pulse intensity for a reduced wavelength to 800 nm would yield almost the identical results.

6.3 Two- and three-dimensional simulations

The RT-bases shock formation and ion acceleration could also be observed in three-dimensional, full PIC simulations. In multidimensional systems, the parameters for the stable shock formation should be different from those in one-dimensional systems, as additional instabilities interrupt the piling up tf the density spike in the early stage. For instance, we observed that the Weibel-like instability [96] grew rapidly for $l_f = 2$ μm, resulting in early destruction of the density spike by severe filamentation. Reducing the interaction time by shortening the front scale length l_f helps to mitigate the filamentation. Also, a gently rising pulse front is known to be effective in keeping the density spike stable for a long time [97]. As another adjustment for robust shock formation, the pulse tail was shortened so that the density spike was less perturbed by the penetrating laser field by RT.

Simulations parameters considering all those factors are $l_f = 0.33$ μm, $l_r = 0.45$ μm, and $n_{max} = 15.6n_c$ (corresponding to $l_0 = 13.7$ nm and $n_0 = 600n_c$ before the explosion), and an asymmetric laser pulse with $a_0 = 16$, pulse rising for 27 fs, falling for 11 fs, and the spot radius 10 μm, respectively. The dimensions of the simulation box were $10 \times 50 \times 50$ [μm] in the X, Y, and Z directions, divided by meshes of 10, 100, and 100 nm in each directions. The simulation results using those parameters are presented in Fig. 6.6. Figure 6.6 (a) is the snapshot of the ion density captured at $t = 120$ fs at which the laser pulse has completely left the plasma. The concentrated region (dark red) of the density represents the shock. From the electric field drawn on the upper plane, it is found that there are two accelerating fields: one is the shock itself, and the other is the sheath. The branch in the ion phase space [Fig. 6.6 (b)] in front of the density spike near the laser axis is a result of velocity doubling by the reflection of incoming ions from the shock front. The number of reflected ions within the laser spot radius 10 μm is $N_{ion} \sim 7 \times 10^{10}$. This value is comparable to the formula $N_{ion} \sim 10^{10}(W_0[\mu m]/\lambda_0[\mu m])$ in Ref. [45], where W_0 is the laser spot radius. The measured efficiency of energy conversion from the laser pulse to the accelerated ions is 4.3%. The Mach number becomes $M < 4$ at $t = 70$ fs and is maintained at around $M \sim 2$ until t = 150 fs [Fig. 6.6 (c)], during which time the ion acceleration continuously takes place. The laser penetration starts at $t = 70$ fs and completes the laser-plasma interaction at t = 113 fs. The slightly distinct second bump above 60 MeV in the ion energy spectrum in Fig. 6.6 (d) takes a similar feature as the one-dimensional result in Fig. 6.2.
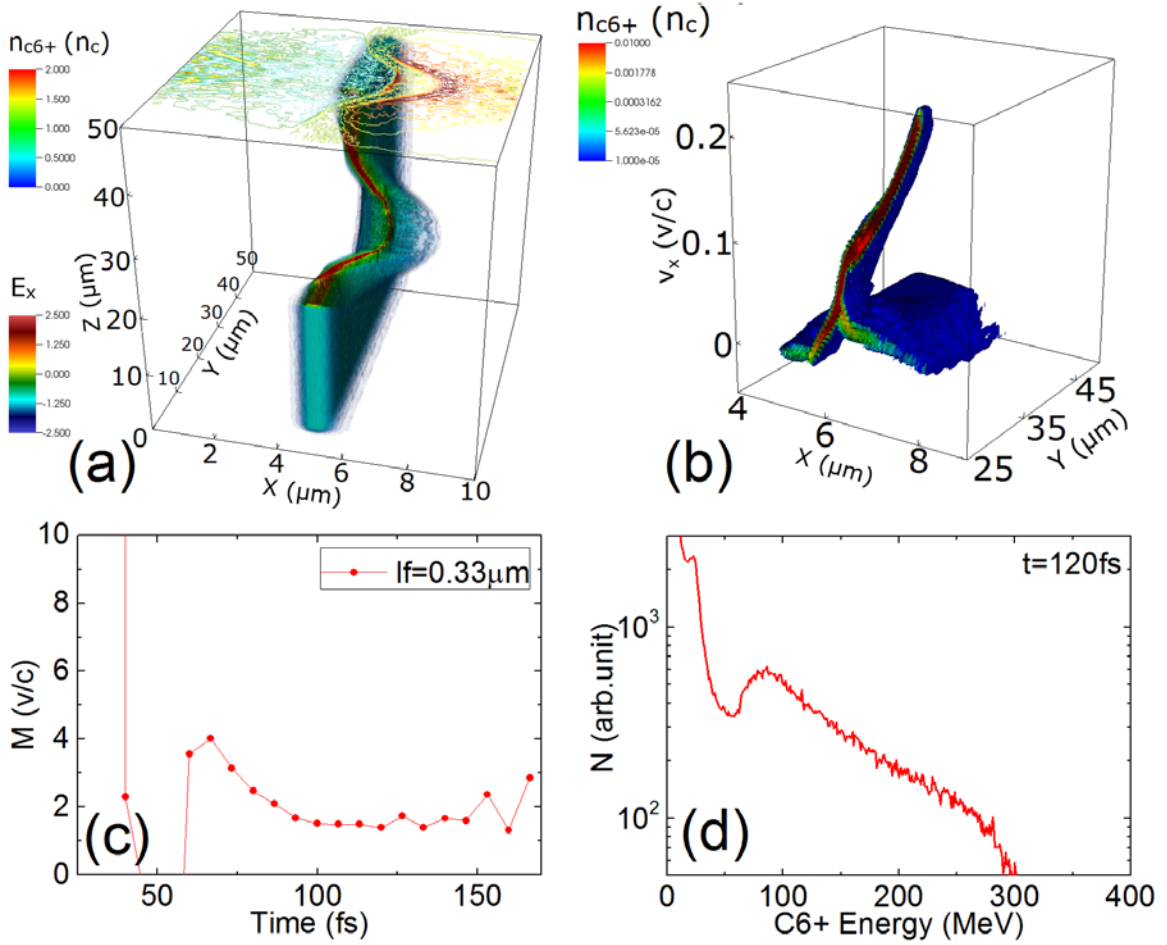
Fig. 6.6: Three dimensional PIC simulation with $a_0 = 16$, circular polarization, $\tau_f = 27$ fs and $\tau_r = 11$ fs, and $l_f = 0.33$ μm. (a) Ion density and longitudinal field E_x on $Z = 25$ μm plane (which is drawn on the upper side of the box) after leaving the laser field at 120 fs. (b) The half cut of a $V_x XY$-phase space of ions. (c) Temporal evolution of the Mach number. (d) Ion energy spectrum at t = 120 fs.

Note that the asymmetric target profile with slightly longer rear side used in the three-dimensional simulation may not be easy to realize in the laboratory. However, the shock is formed dominantly in the front side, so the rear side dimension is not so influential. The rear side tail, as described in Ref. [28], is used usually for the sheath control. As the sheath effect can be suppressed by a longer tail in the rear, the symmetric target with a shorter l_f in out three-dimensional simulation should have resulted in slightly increased maximum energy of ions and more energy spread by the increased sheath effect.

6.4 Conclusion

In conclusion, by one- and three-dimensional PIC simulations, we revealed a new procedure of electrostatic shock formation by relativistic transparency (RT) in exploded targets and related ion

acceleration. In this procedure, the penetrating laser field by RT rapidly heats up the electron plasma, providing the upstream with the condition of high sound speed. Reduction of the target plasma density ro induce RT of a *circularly* polarized pulse could be achieved by expansion of the exploded targets. The partially reflecting portion of the pulse drives an initial density spike to piston velocity via the hole-boring mechanism. When the reflected and transparent portions of the driving pulse are properly chosen, the Mach number of the initial density spike satisfies the shock criterion, i.e., $M > 1.5$, turning it into an electrostatic shock. The shock could be sustained for a long time even in the absence of the driving pulse, owing to the tapered density of the expanded target. The ions in the upstream are reflected from the shock front to constitute a localized energetic ion bunce. In a certain case the shock front itself contained a monoenergetic portion of the ions.

The rapid electron heating by the transparent field allows the use of a short driving pulse of a few tens of femtoseconds. Using a circularly polarized pulse significantly relaxes the demands for high pulse power required for compression of the initial density spike, i.e., down to 1 PW (or slightly larger). Ti:sapphire laser systems with those parameters are readily available with contemporary technology. Furthermore the controlled ASE or prepulse is utilized for target explosion to induce a suitable RT. The relativistic transparency can be controlled by using the target expansion level, which is possible in the experiment using ASE or a prepulse, or by changing the initial target thickness for a given ASE. Those specifications envisage a new parameter regime of shock ion acceleration.

7. Summary

In summary, we introduced background for understand laser-driven ion acceleration such as history, basic plasma physics, ponderomotive force, and representative regimes. Among them, the characteristic of ponderomotive force depending on polarization is especially important to understand overall feature of our research. Oscillating ponderomotive force of LP pulse generates hot electrons via JxB heating and non-oscillating ponderomotive force of CP pulse effectively compresses plasma without significant heating.

A parametric study of TNSA using double layer target serves information of independence between the areal density of the second layer and the thickness of the first layer on accelerated proton beam. This topic has a meaning of confirmation of the relationship. In addition, it helps us to understand TNSA and its simulation in detail.

We strictly discovered electrostatic shock ion acceleration using CP pulse for the first time. Relativistic transparency should be required to heat up upstream temperature by CP pulse, whereas RT does not be required to increase temperature due to JxB heating when LP pulse drives shock. On behalf of better ability of CP pulse in density compression, CP-driven shock is possible in lower density plasma then LP-driven shock. It results in higher hole-boring velocity and energetic ion beam with respect to the same total energy of LP pulse.

References

[1] D. Strickland and G. Mourou, Opt. Commun. **56**, 219 (1985).

[2] V. Malka, S. Fritzler, E. Lefebvre, E. d'Humières, R. Ferrand, G. Grillon, C. Albaret, S. Meyroneinc, J.-P. Chambaret, A. Antonetti and D. Hulin, Med. Phys. **31**, 1587 (2004).

[3] E. Fourkal, I. Velchev, J. Fan, W. Luo and C.-M. Ma, Med. Phys. **34**, 577 (2007).

[4] S. V. Bulanov, T. Zh. Esirkepov, V. S. Khoroshkov, A. V. Kuznetsov and F. Pegoraro, Phys. Lett. A **299**, 240 (2002).

[5] M. Borghesi, A. Schiavi, D. H. Campbell, M. G. Haines, O. Willi, A. J. MacKinnon, L. A. Gizzi, M. Galimberti, R. J. Clarke and H. Ruhl, Plasma Phys. Control. Fusion **43**, A267 (2001).

[6] C. A. Cecchetti, M. Borghesi, J. Fuchs, G. Schurtz, S. Kar, A. Macchi, L. Romagnani, P. A. Wilson, P. Antici, R. Jung, J. Osterholtz, C. A. Pipahl, O. Willi, A. Schiavi, M. Notley, and D. Neely, Phys. Plasmas **16**, 043102 (2009).

[7] J. Alvarez, J. Fernández-Tobias, K. Mima, S. Nakai, S. Kar, Y. Kato, J. M. Perlado, Phys. Proc. **60**, 29 (2014).

[8] P. McKenna, K.W. D. Ledingham, T. McCanny, R. P. Singhal, I. Spencer, M. I. K. Santala, F. N. Beg, K. Krushelnick, M. Tatarakis, M. S.Wei, E. L. Clark, R. J. Clarke, K. L. Lancaster, P. A. Norreys, K. Spohr, R. Chapman, and M. Zepf, Phys. Rev. Lett. **91**, 075006 (2003).

[9] I. Spencer, K. W. D. Ledingham, R. P. Singhal, T. McCanny, P. McKenna, E. L. Clark, K. Krushelnick, M. Zepf, F. N. Beg, M. Tatarakis, A. E. Dangor, P. A. Norreys, R. J. Clarke, R. M. Allott, and I. N. Ross, Nucl. Instrum. Meth. in Phys. Res. B **183**, 449 (2001).

[10] K. Krushelnick, E. L. Clark, R. Allott, F. N. Beg, C. N. Danson, A. Machacek, V. Malka, Z. Najmudin, D. Neely, P. A. Norreys, M. R. Salvati, M. I. K. Santala, M. Tatarakis, I. Watts, M. Zepf, and A. E. Dangor, IEEE Tran. on Plas. Sci. **28**, 1110 (2000).

[11] J. C. Fernández, J.J. Honrubia, B. J. Albright, K. A. Flippo, D. C. Gautier, B. M. Hegelich, Mark J. Schmitt, M. Temporal, and Lin Yin, Nucl. Fusion **49**, 065004 (2009).

[12] B. I. Cho, G. M. Dyer, S. Kneip, S. Pikuz, D. R. Symes, A. C. Bernstein, Y. Sentoku, N. Renard-Le Galloudec, T. E. Cowan, and T. Ditmire, Phys. Plasmas **15**, 052701 (2008).

[13] A. Stockem, T. Grismayer, R. A. Fonseca, and L. O. Silva, Phys. Rev. Lett. **113**, 105002 (2014).

[14] U. Masood, M. Bussmann, T. E. Cowan, W. Enghardt, L. Karsch, F. Kroll, U. Schramm and J. Pawelke, Appl. Phys. B **117**, 41 (2014).

[15] T. E. Cowan, J. Fuchs, H. Ruhl, A. Kemp, P. Audebert, M. Roth, R. Stephens, I. Barton, A. Blazevic, E. Brambrink, J. Cobble, J. Fernández, J.-C. Gauthier, M. Geissel, M. Hegelich, J. Kaae, S. Karsch, G. P. Le Sage, S. Letzring, M. Manclossi, S. Meyroneinc, A. Newkirk, H. Pépin, and N. Renard-LeGalloudec, Phys. Rev. Lett. **92**, 204801 (2004).

[16] R. A. Snavely, M. H. Key, S. P. Hatchett, T. E. Cowan, M. Roth, T.W. Phillips, M. A. Stoyer, E.

A. Henry, T. C. Sangster, M. S. Singh, S. C. Wilks, A. MacKinnon, A. Offenberger, D.M. Pennington, K. Yasuike, A. B. Langdon, B. F. Lasinski, J. Johnson, M. D. Perry, and E. M. Campbell, Phys. Rev. Lett. **85**, 2945 (2000).

[17] T.E. Cowan, M. Roth, J. Johnson, C. Brown, M. Christl, W. Fountain, S. Hatchett, E.A. Henry, A.W. Hunt, M.H. Key, A. MacKinnon, T. Parnell, D.M. Pennington, M.D. Perry, T.W. Phillips, T.C. Sangster, M. Singh, R. Snavely, M. Stoyer, Y. Takahashi, S.C. Wilks, and K. Yasuike, Nucl. Inst. Methods in Phys. Research A **455** 130 (2000).

[18] A. Maksimchuk, S. Gu, K. Flippo, and D. Umstadter, Phys. Rev. Lett. **84**, 4108 (2000).

[19] A. J. Mackinnon, Y. Sentoku, P. K. Patel, D.W. Price, S. Hatchett, M. H. Key, C. Andersen, R. Snavely, and R. R. Freeman, Phys. Rev. Lett. **88**, 215006 (2002).

[20] M. Allen, P. K. Patel, A. Mackinnon, D. Price, S. Wilks, and E. Morse, Phys. Rev. Lett. **93**, 265004 (2004).

[21] S. C. Wilks, A. B. Langdon, T. E. Cowan, M. Roth, M. Singh, S. Hatchett, M. H. Key, D. Pennington, A. MacKinnon and R. A. Snavely, Phys. Plasmas **8**, 542 (2001).

[22] P. Mora, Phys. Rev. Lett. **90**, 185002 (2003).

[23] L. Robson, P. T. Simpson, R. J. Clarke, K. W. D. Ledingham, F. Lindau, O. Lundh, T. McCanny, P. Mora, D. Neely, C. G. Wahlstrom, M. Zepf and P. McKenna, Nat. Phys. **3**, 58-62 (2007).

[24] M. Passoni, and M. Lontano, Phys. Rev. Lett. **101**, 115001 (2008).

[25] M. Passoni, L. Bertagna, and A. Zani, New J. Phys. **12,** 045012 (2010).

[26] H. Schwoerer, S. Pfotenhauer, O. Jackel, K. U. Amthor, B. Liesfeld, W. Ziegler, R. Sauerbrey, K. W. D. Ledingham and T. Esirkepov, Nature **439**, 445-448 (2006).

[27] B. M. Hegelich, B. J. Albright, J. Cobble, K. Flippo, S. Letzring, M. Paffett, H. Ruhl, J. Schreiber, R. K. Schulze and J. C. Fernández, Nature **439**, 441 (2006).

[28] A. Macchi, F. Cattani, T. V. Liseykina, and F. Cornolti, Phys. Rev. Lett. **94**, 165003 (2005).

[29] M. Chen, A. Pukhov, Z. M. Sheng, and X. Q. Yan, Phys. Plasmas **15**, 113103 (2008).

[30] O. Klimo, J. Psikal, J. Limpouch and V. T. Tikhonchuk, Phys. Rev. Spec. Top-Ac **11**, 031301 (2008).

[31] A P L Robinson, M Zepf, S Kar, R G Evans, and C Bellei, New J. Phys. **10,** 013021 (2008).

[32] A P L Robinson, D-H Kwon, and K Lancaster, Plasma Phys. Control. Fusion **51,** 095006 (2009).

[33] A P L Robinson, P Gibbon, M Zepf, S Kar, R G Evans, and C Bellei, Plasma Phys. Control. Fusion **51,** 024004 (2009).

[34] T.P. YU, M. CHEN, and A. PUKHOV, Laser and Part. Beams **27**, 611 (2009).

[35] B. Qiao, M. Zepf, M. Borghesi and M. Geissler, Phys. Rev. Lett. **102**, 145002 (2009).

[36] M. Chen, A. Pukhov, T. P. Yu, and Z. M. Sheng, Phys. Rev. Lett. **103**, 024801 (2009).

[37] A. Macchi, S. Veghini, and F. Pegoraro, Phys. Rev. Lett. **103**, 085003 (2009).

[38] A. Henig, S. Steinke, M. Schnurer, T. Sokollik, R. Horlein, D. Kiefer, D. Jung, J. Schreiber, B. M. Hegelich, X. Q. Yan, J. Meyer-ter-Vehn, T. Tajima, P. V. Nickles, W. Sandner and D. Habs, Phys. Rev. Lett. **103**, 254003 (2009).

[39] B. Qiao, M. Zepf, M. Borghesi, B. Dromey, M. Geissler, A. Karmakar, and P. Gibbon, Phys. Rev. Lett. **105**, 155002 (2010).

[40] S. Kar, K. F. Kakolee, B. Qiao, A. Macchi, M. Cerchez, D. Doria, M. Geissler, P. McKenna, D. Neely, J. Osterholz, R. Prasad, K. Quinn, B. Ramakrishna, G. Sarri, O.Willi, X.Y. Yuan, M. Zepf, and M. Borghesi, Phys. Rev. Lett. **109**, 185006 (2012).

[41] A. Macchi, S. Veghini, T. V. Liseykina, and F. Pegoraro, New J. Phys. **12**, 045013 (2010).

[42] W. P. Wang, B. F. Shen, X. M. Zhang, L. L. Ji, M. Wen, J. C. Xu, Y. H. Yu, Y. L. Li, and Z. Z. Xu, Phys. Plasmas **18**, 013103 (2011).

[43] C. A. J. Palmer, N. P. Dover, I. Pogorelsky, M. Babzien, G. I. Dudnikova, M. Ispiriyan, M. N. Polyanskiy, J. Schreiber, P. Shkolnikov, V. Yakimenko and Z. Najmudin, Phys. Rev. Lett. **106**, 014801 (2011).

[44] N. P. Dover and Z. Najmudin, High Energy Density Physics **8**, 170 (2012)

[45] L. O. Silva, M. Marti, J. R. Davies and R. A. Fonseca, Phys. Rev. Lett. **92**, 015002 (2004).

[46] T. Nakamura, and K. Mima, Phys. Rev. Lett. **100**, 205006 (2008).

[47] T. Nakamura, S. V. Bulanov, T. Zh. Esirkepov, and M. Kando, Phys. Rev. Lett. **105**, 135002 (2010).

[48] S. S. Bulanov, V. Yu. Bychenkov, V. Chvykov, G. Kalinchenko, D. W. Litzenberg, T. Matsuoka, A. G. R. Thomas, L. Willingale, V. Yanovsky, K. Krushelnick, and A. Maksimchuk, Phys. Plasmas **17**, 043105 (2010).

[49] L. Yin, B. J. Albright, B. M. Hegelich, K. J. Bowers, K. A. Flippo, T. J. T. Kwan, and J. C. Fernández, Phys. Plasmas **14**, 056706 (2007).

[50] B. J. Albright, L. Yin, K. J. Bowers, B. M. Hegelich, K. A. Flippo, T. J. T. Kwan, and J. C. Fernández, Phys. Plasmas **14**, 094502 (2007).

[51] C. Curry, M. Gauthier, R. Mishra, J. Kim, S. Goede, A. Propp, F. Fiuza, S. H. Glenzer, J. Williams, C. Goyon, A. E. Pak, S. Kerr, Y. Y. Tsui, B. Ramakrishna, B. Aurand, O. Willi and C. Roedel, 57th Annu. Meet. of the APS Divi. of Plas. Physics 60, 19 (2015).

[52] M. H. Helle, D. F. Gordon, D. Kaganovich, Y. Chen, J. P. Palastro and A. Ting, e-print arXiv:1507.04594.

[53] P. L. Poole, C. D. Andereck, D. W. Schumacher, R. L. Daskalova, S. Feister, K. M. George, C. Willis, K. U. Akli, and E. A. Chowdhury, Phys. Plasmas **21**, 063109 (2014).

[54] F. F. Chen, *Introduction to Plasma Physics and Controlled Fusion* vol. 1: Springer, 2006.

[55] T. J. Yu, S. K. Lee, J. H. Sung, J. W. Yoon, T. M. Jeong, and J. M. Lee, Opt. Express **20**, 10807

(2012).

[56] H. Daido, M. Nishiuchi, and A. S. Pirozhkov, Rep. Prog. Physics. **75**, 056401 (2012).

[57] D. Neely, P. Foster, A. Robinson, F. Lindau, O. Lundh, A. Persson, C.-G. Wahlström, and P. McKenna, Appl. Phys. Lett, **89**, 021502 (2006).

[58] M. Kaluza, J. Schreiber, M. I. K. Santala, G. D. Tsakiris, K. Eidmann, J. Meyer-ter-Vehn, and K. J.Witte, Phys. Rev. Lett. **93**, 045003 (2004).

[59] A. J. Mackinnon, M. Borghesi, S. Hatchett, M. H. Key, P. K. Patel, H. Campbell, A. Schiavi, R. Snavely, S. C. Wilks, and O. Willi, Phys. Rev. Lett. **86**, 1769 (2002).

[60] K. Matsukado, T. Esirkepov, K. Kinoshita, H. Daido, T. Utsumi, Z. Li, A. Fukumi, Y. Hayashi, S. Orimo, M. Nishiuchi, S.V. Bulanov, T. Tajima, A. Noda, Y. Iwashita, T. Shirai, T. Takeuchi, S. Nakamura, A. Yamazaki, M. Ikegami, T. Mihara, A. Morita, M. Uesaka, K. Yoshii, T.Watanabe, T. Hosokai, A. Zhidkov, A. Ogata, Y.Wada, and T. Kubota, Phys. Rev. Lett. **91**, 215001 (2003).

[61] J. Fuchs, Y. Sentoku, E. d'Humieres, T. E. Cowan, J. Cobble, P. Audebert, A. Kemp, A. Nikroo, P. Antici, E. Brambrink, A. Blazevic, E. M. Campbell, J. C. Fernandez, J. C. Gauthier, M. Geissel, M. Hegelich, S. Karsch, H. Popescu, N. Renard-LeGalloudec, M. Roth, J. Schreiber, R. Stephens and H. Pepin, Phys. Plasmas **14**, 053105 (2007).

[62] A. Macchi, A. S. Nindrayog and F. Pegoraro, Phys. Rev. E **85**, 046402 (2012).

[63] J. Fuchs, P. Antici, E. D'Humieres, E. Lefebvre, M. Borghesi, E. Brambrink, C. A. Cecchetti, M. Kaluza, V. Malka, M. Manclossi, S. Meyroneinc, P. Mora, J. Schreiber, T. Toncian, H. Pepin and R. Audebert, Nat. Phys. **2**, 48-54 (2006).

[64] J. Badziak, E. Woryna, R. Parys, K. Y. Platonov, S. Jablonski, L. Rye, A. B. Vankov and J. Wolowski, Phys. Rev. Lett. **87**, 215001 (2001).

[65] T. Z. Esirkepov, S. V. Bulanov, K. Nishihara, T. Tajima, F. Pegoraro, V. S. Khoroshkov, K. Mima, H. Daido, Y. Kato, Y. Kitagawa, K. Nagai and S. Sakabe, Phys. Rev. Lett. **89**, 175003 (2002).

[66] Z. Lecz, O. Boine-Frankenheim and V. Kornilov, Nucl. Instrum. Meth. A **727**, 51-58 (2013).

[67] A. V. Brantov, V. T. Tikhonchuk, V. Y. Bychenkov and S. G. Bochkarev, Phys. Plasmas **16**, 043107 (2009).

[68] E. Fourkal, I. Velchev and C. M. Ma, Phys. Rev. E **71**, 036412 (2005).

[69] T. Esirkepov, M. Yamagiwa and T. Tajima, Phys. Rev. Lett. **96**, 105001 (2006).

[70] J. Q. Yu, X. L. Jin, W. M. Zhou, B. Zhang, Z. Q. Zhao, L. F. Cao, B. Li, Y. Q. Gu, R. X. Zhan and Z. Najmudin, Laser Part. Beams **31**, 597-605 (2013).

[71] J. Q. Yu, X. L. Jin, W. M. Zhou, Y. Q. Gu, R. X. Zhan, Z. Q. Zhao, L. F. Cao and B. Li, High Energy Density Phys. **9**, 745-749 (2013).

[72] A.P.L. Robinson, A.R. Bell, R.J. Kingham, Phys. Rev. Lett. **96**, 035005 (2006).

[73] A. Ulman, Chem. Rev. **96**, 1533-1554 (1996).

[74] Wu, H. C. "JPIC How to make a PIC code." arXiv:1104.3163.(2011)

[75] Y. Sentoku, T. E. Cowan, A. Kemp and H. Ruhl, Phys. Plasmas **10**, 2009-2015 (2003).

[76] M. G. Haines, M. S. Wei, F. N. Beg and R. B. Stephens, Phys. Rev. Lett. **102**, 045008 (2009).

[77] Y. Sentoku, V. Y. Bychenkov, K. Flippo, A. Maksimchuk, K. Mima, G. Mourou, Z. M. Sheng and D. Umstadter, Appl. Phys. B-Lasers. Opt. **74**, 207-215 (2002).

[78] L. Torrisi, S. Gammino, A. M. Mezzaslma, J. Badziak, P. Parys, J. Wolowski, E. Woryna, J. Krása, L. Láska, M. Pfeifer, K. Rohlena and F. P. Boody, Appl. Surf. Sci. **217**, 319 (2003).

[79] F. P. Boody, R. Höpfl, H. Hora and J. C. Kelly, Laser and Particle Beams **14**, 443 (1996).

[80] I. J. Kim, K. H. Pae, C. M. Kim, H. T. Kim, J. H. Sung, S. K. Lee, T. H. Yu, I. W. Choi, C.-L. Lee, K. H. Nam, P. V. Nickles, T. M. Jeong and J. M. Lee, Phys. Rev. Lett.**111**, 165003 (2013).

[81] M. Chen, Z.-M. Sheng, Q.-L. Dong, M.-Q. He, S.-M. Weng, Y.-T. Li and J. Zhang, Phys. Plasmas **14**, 113106 (2007).

[82] H. Y. Wang, C. Lin, B. Liu, Z. M. Sheng, H. Y. Lu, W. J. Ma, J. H. Bin, J. Schreiber, X. T. He, J. E. Chen, M. Zepf and X. Q. Yan, Phys. Rev. E **89**, 013107 (2014).

[83] A. Zhidkov, M. Uesaka, A. Sasaki and H. Daido, Phys. Rev. Lett **89**, 215002 (2002).

[84] F. Fiuza, A. Stockem, E. Boella, R. A. Fonseca, L. O. Silva, D. Haberberger, S. Tochitsky, C. Gong, W. B. Mori and C. Joshi, Phys. Rev. Lett. **109**, 215001 (2012).

[85] D. Haberberger, S. Tochitsky, F. Fiuza, C. Gong, R. A. Fonseca, L. O. Silva, W. B. Mori and C. Joshi, Nat. Physics **8** 95, (2012).

[86] H. Zhang, B. F. Shen, W. P. Wang, Y. Xu, Y. Q. Liu, X. Y. Liang, Y. X. Leng, R. X. Li, X. Q. Yan, J. E. Chen and Z. Z. Xu, Phys. Plasmas **22**, 013113 (2015).

[87] D. W. Forslund and C. R. Shonk, Phys. Rev. Lett. **25**, 1699 (1970).

[88] C. A. J. Palmer, N. P. Dover, I. Pogorelsky, M. Babzien, G. I. Dudnikova, M. Ispiriyan, M. N. Polyanskiy, J. Schreiber, P. Shkolnikov, V. Yakimenko and Z. Najmudin, Phys. Rev. Lett. **106**, 014801 (2011).

[89] A. A. Andreev, S. Steinke, T. Sokollik, M. Schnűrer and S. T. Avetsiyan, Phys. Plasmas **16**, 013103 (2009).

[90] A. Yogo, H. Daido, S. V. Bulanov, K. Nemoto, Y. Oishi, T. Nayuki, T. Fujii, K. Ogura, S. Orimo, A. Sagisaka, J.-L. Ma, T. Zh. Esirkepov, M. Mori, M. Nishiuchi, A. S. Pirozhkov, S. Nakamura, A. Noda, H. Nagatomo, T. Kimura and T. Tajima, Phys. Rev. E **77**, 016401 (2008).

[91] E. d'Humières, P. Antici, M. Glesser, J. Boeker, F. Cardelli, S. Chen, J.L. Feugeas, F. Filippi, M. Gauthier, A. Levy, P. Nicolaï, H. Pépin, L. Romagnani, M. Sciscìò, V. T. Tikhonchuk, O. Willi, J.C. Kieffer, and J. Fuchs, Plasma Phys. Control. Fusion **55**, 124025 (2013).

[92] L. Yin, B. J. Albright, D. Jung, K. J. Bowers, R. C. Shah, S. Palaniyappan, J. C. Fernández and B. M. Hegelich, Phys. Plasmas **18**, 053103 (2011).

[93] I. H. Nam, M. S. Hur, H. S. Uhm, N. A. M. Hafz and H. Y. Suk, Phys. Plasmas **18**, 043107 (2011).

[94] M. S. Hur, Y.-K. Kim, V. V. Kulagin, I. H. Nam and H. Y. Suk, Phys. Plasmas **19**, 073114 (2012).

[95] M.-H. Cho, Y.-K. Kim and M. S. Hur, Phys. Plasmas **20**, 093112 (2013).

[96] X. M. Zhang, B. F. Shen, L. L. Ji, W. P. Wang, J. C. Xu, Y. H. Yu and X. F. Wang, Phys. Plasmas **18**, 073101 (2011).

[97] L. L. Ji, B. F. Shen, X. M. Zhang, F. C. Wang, Z. Y. Jin, X. M. Li, M. Wen and J. R. Cary, Phys. Rev. Lett **101** 164802 (2008).

[98] S. C. Chapra, *Applied Numerical Methods with Matlab* Second Edition: Mc Graw Hill, 2008.

[99] Y. Wenhua, M. Raj, and S. Tao, *Parallel Finite-Difference Time-Domain Method*: Artech House, 2006.